O.V. Lounasmaa Laboratory

Microscopic and Macroscopic Studies of Liquid and Solid Helium Mixtures

Juho Rysti

Aalto University

DOCTORAL DISSERTATIONS

Aalto University publication series
DOCTORAL DISSERTATIONS 110/2013

Microscopic and Macroscopic Studies of Liquid and Solid Helium Mixtures

Juho Rysti

A doctoral dissertation completed for the degree of Doctor of Science (Technology) to be defended, with the permission of the Aalto University School of Science, at a public examination held at the lecture hall E of the school on 19 August 2013 at 12.

Aalto University
School of Science
O.V. Lounasmaa Laboratory
YKI group

Supervising professor
Prof. Pertti Hakonen

Thesis advisor
Doc. Juha Tuoriniemi

Preliminary examiners
Dr. Finn Berg Rasmussen, University of Copenhagen, Denmark
Doc. Mikko Saarela, University of Oulu, Finland

Opponent
Prof. Jeevak Parpia, Cornell University, United States of America

Aalto University publication series
DOCTORAL DISSERTATIONS 110/2013

ISBN 978-952-60-5244-1 (printed)
ISBN 978-952-60-5245-8 (pdf)
ISSN-L 1799-4934
ISSN 1799-4934 (printed)
ISSN 1799-4942 (pdf)
http://urn.fi/URN:ISBN:978-952-60-5245-8

Unigrafia Oy
Helsinki 2013

Finland

441 697
Printed matter

Aalto University

Abstract

Aalto University, P.O. Box 11000, FI-00076 Aalto www.aalto.fi

Author
Juho Rysti

Name of the doctoral dissertation
Microscopic and Macroscopic Studies of Liquid and Solid Helium Mixtures

Publisher School of Science

Unit O.V. Lounasmaa Laboratory

Series Aalto University publication series DOCTORAL DISSERTATIONS 110/2013

Field of research Engineering Physics, Physics

Manuscript submitted 16 April 2013 **Date of the defence** 19 August 2013

Permission to publish granted (date) 31 May 2013 **Language** English

☐ **Monograph** ☒ **Article dissertation (summary + original articles)**

Abstract

At low temperatures, helium offers a unique system for the study of quantum mechanical effects on a macroscopic scale. It is the only known condensed matter system, which remains liquid down to the absolute zero temperature. For this reason, helium forms a unique quantum liquid, which can be studied in laboratory conditions. The two stable isotopes of helium, ^{3}He and ^{4}He, obey the two different quantum statistics, ^{3}He being a fermion and ^{4}He a boson. They both undergo a transition into a superfluid state at low temperatures. A new interesting system is obtained by mixing the isotopes. Remarkably, ^{3}He has a finite solubility in ^{4}He even at zero temperature. Dual Fermi-Bose superfluidity of helium mixtures has been predicted to exist, but it has not been observed experimentally. The difficulty is the required extremely low temperature.

Adiabatic melting of solid ^{4}He in the presence of liquid ^{3}He is a promising new cooling technique, which is hoped to produce the superfluid transition of helium mixtures. We have been preparing an experiment, which would implement this concept, but due to the complicated experimental setup, we have not yet been able to harvest the full power of the method. The results of this thesis revolve around supporting work for this experiment. In the course of the present studies, some aspects have generated deeper interest in their own right.

In this thesis properties of liquid and solid helium mixtures are studied computationally and experimentally. Interactions between ^{3}He atoms dissolved in superfluid ^{4}He are investigated by analyzing experimental data. These interactions determine the transition temperature of the relished superfluid state of helium mixtures. The obtained model for the interactions is further used to calculate other quantities of interest. Retrieving the properties of liquid helium requires novel tools. One such tool, which was introduced to helium research not too long ago, is the quartz tuning fork. It is a mechanical oscillator, whose resonant behavior depends on the surrounding fluid environment. Its complicated geometry presents difficulty in analyzing its characteristics. Numerical methods are utilized in this thesis to understand effects of liquid helium on the quartz tuning fork response.

Keywords helium-3, helium-4, helium mixtures, superfluid, melting pressure, solubility, osmotic pressure, quartz tuning fork, acoustic emission, second sound

ISBN (printed) 978-952-60-5244-1 **ISBN (pdf)** 978-952-60-5245-8

ISSN-L 1799-4934 **ISSN (printed)** 1799-4934 **ISSN (pdf)** 1799-4942

Location of publisher Helsinki **Location of printing** Helsinki **Year** 2013

Pages 198 **urn** http://urn.fi/URN:ISBN:978-952-60-5245-8

Tekijä
Juho Rysti

Väitöskirjan nimi
Mikroskooppisia ja makroskooppisia tutkimuksia nestemäisissä ja kiinteissä heliumseoksissa

Julkaisija Perustieteiden korkeakoulu

Yksikkö O.V. Lounasmaa -laboratorio

Sarja Aalto University publication series DOCTORAL DISSERTATIONS 110/2013

Tutkimusala Teknillinen fysiikka, fysiikka

Käsikirjoituksen pvm 16.04.2013 **Väitöspäivä** 19.08.2013

Julkaisuluvan myöntämispäivä 31.05.2013 **Kieli** Englanti

☐ **Monografia** ☒ **Yhdistelmäväitöskirja (yhteenveto-osa + erillisartikkelit)**

Tiivistelmä

Matalissa lämpötiloissa helium on ainutlaatuinen systeemi kvanttimekaanisten ilmiöiden tutkimiseen makroskooppisessa mittakaavassa. Se on ainut tunnettu systeemi, joka pysyy nesteenä lämpötilan absoluuttiseen nollapisteeseen asti. Tästä johtuen heliumista muodostuu ainutlaatuinen kvanttineste, jota voidaan tutkia laboratorio-olosuhteissa. Heliumin kaksi vakaata isotooppia, ^{3}He ja ^{4}He, noudattavat kahta eri kvanttistatistiikkaa, ^{3}He:n ollessa fermioni ja ^{4}He:n bosoni. Molemmat muuttuvat supranesteiksi matalissa lämpötiloissa. Uusi mielenkiintoinen systeemi saadaan aikaiseksi sekoittamalla näitä isotooppeja. Yllättäen ^{3}He liukenee ^{4}He:än jopa absoluuttisessa nollapisteessä. Heliumseoksen fermioni-bosoni -kaksoissupranesteen on ennustettu olevan olemassa, mutta sitä ei ole vielä havaittu kokeellisesti. Vaikeutena sen saavuttamisessa on tarvittava lämpötila, joka on äärimmäisen matala.

Helium-4:n adiabaattinen sulatus ^{3}He:n joukkoon on uusi lupaava jäähdytystekniikka, jonka toivotaan mahdollistavan heliumseosten suprajuoksevuuden saavuttamisen. Olemme valmistelleet koetta, jossa käytettäisiin tätä menetelmää, mutta monimutkaisen koejärjestelyn vuoksi emme ole vielä päässeet hyödyntämään sen täyttä potentiaalia. Tämän väitöskirjan tulokset liittyvät kyseistä koetta tukevaan työhön. Tutkimusten edetessä jotkin osa-alueet ovat muodostuneet itsessään mielenkiintoisiksi tutkimuskohteiksi.

Tässä väitöskirjassa nestemäisten ja kiinteiden heliumseosten ominaisuuksia tutkitaan laskennallisesti ja kokeellisesti. Helium-3 -atomien välisiä vuorovaikutuksia ^{4}He:ssä tarkastellaan analysoimalla kokeellisia tuloksia. Nämä vuorovaikutukset määräävät lämpötilan, jossa heliumseos muodostaa odotetun supranestetilan. Saadulla vuorovaikutusten mallilla lasketaan myös muita hyödyllisiä ominaisuuksia. Heliumin ominaisuuksien tutkiminen vaatii uudenlaisia työkaluja. Eräs tällainen työkalu, joka on melko uusi heliumtutkimuksessa, on ääniraudan muotoinen kvartsivärähtelijä. Se on mekaaninen värähtelijä, jonka resonanssiominaisuudet riippuvat ympäröivän aineen ominaisuuksista. Näiden värähtelijöiden monimutkainen geometria vaikeuttaa niiden värähtelyominaisuuksien tarkastelua. Tässä väitöskirjassa tutkitaan nestemäisen heliumin vaikutuksia kvartsivärähtelijöihin numeerisin menetelmin.

Avainsanat helium-3, helium-4, heliumseos, supraneste, sulamispaine, liukoisuus, osmoottinen paine, kvartsivärähtelijä, akustinen emissio, toinen ääni

ISBN (painettu) 978-952-60-5244-1 **ISBN (pdf)** 978-952-60-5245-8

ISSN-L 1799-4934 **ISSN (painettu)** 1799-4934 **ISSN (pdf)** 1799-4942

Julkaisupaikka Helsinki **Painopaikka** Helsinki **Vuosi** 2013

Sivumäärä 198 **urn** http://urn.fi/URN:ISBN:978-952-60-5245-8

Contents

Acknowledgments

The work presented in this doctoral thesis has been performed in the YKI group of O.V. Lounasmaa Laboratory (Low Temperature Laboratory) of Aalto University (formerly Helsinki University of Technology). Many people have had direct and/or indirect contribution to this thesis, but here I can only express my gratitude to a small subset of these people. I am grateful to the previous director of the laboratory, Professor Mikko Paalanen, for creating a great atmosphere for high-quality research and for many pleasant conversations. I thank my supervisor and current director, Professor Pertti Hakonen, for helping with the bureaucracy involved and for taking over the leadership of the laboratory in a challenging situation.

I had very ambitious plans for the contents of my thesis. Carrying out all those things and publishing the results would have postponed my graduation considerably. I thank Professor Matti Kaivola, my former supervisor, for explaining to me that in the academic world a doctoral degree is not much more than a "driver's license", which one must acquire. This inspired me to choose the route of faster graduation, despite leaving me far from a feeling of perfection toward this thesis.

Textbooks teach the known things about physics, but not really how to do research, write publications, etc. The certain kind of maturity required in studying how nature works comes only through experience. Guidance by an experienced researcher is of great aid to a graduate student in his struggle to learn these subtle skills. Consequently my deepest gratitude regarding this thesis and my graduate studies belongs to my instructor and leader of the YKI group, Docent Juha Tuoriniemi. He has spent countless hours guiding me, explaining the oddities of low temperature phenomena, and discussing physics in general. I also thank him for allowing me to have strong influence on my projects over the years. I feel lucky to have been able to try it all: experimental, theoretical, and numerical work.

Previous and current graduate students of our group, Dr. Elias Pentti, Dr. Anssi Salmela, and M.Sc. Matti Manninen, have been of great help and this thesis

has directly benefited from their contributions. I have had many useful discussions with Dr. Alexander Sebedash and Dr. Igor Todoshchenko. I also want to acknowledge former undergraduate students M.Sc. Jukka-Pekka Kaikkonen and B.Sc. Ville Peri. The assistance of the secretaries and workshop personnel has been invaluable throughout my time in the lab. Over the years I have had many interesting discussions, both physics-related and -unrelated, with Professor Matti Krusius, Dr. Risto Hänninen, Dr. Jaakko Hosio, M.Sc. Petri Heikkinen, and B.Sc. Tapio Riekki, to name but a few. Fellow students and other staff members have made O.V. Lounasmaa Laboratory a convivial place to work at.

Finally, and most importantly, I thank my family for their support and understanding throughout the years.

List of publications

This Thesis consists of an introductory part and the publications listed below. The introductory part includes some previously unpublished material.

I J. Rysti, J. Tuoriniemi, and A. Salmela. *Effective ^{3}He interactions in dilute ^{3}He–^{4}He mixtures*. Physical Review B **85**, 134529 (2012).

II Anssi Salmela, Alexander Sebedash, Juho Rysti, Elias Pentti, and Juha Tuoriniemi. *Osmotic pressure of ^{3}He/ ^{4}He mixtures at the crystallization pressure and at millikelvin temperatures*. Physical Review B **83**, 134510 (2011).

III J Rysti, J Tuoriniemi, A Salmela, and A Sebedash. *Melting pressure of saturated helium mixture at temperatures between 10 mK and 0.5 K*. Journal of Physics: Conference Series **400**, 012065 (2012).

IV Elias Pentti, Juho Rysti, Anssi Salmela, Alexander Sebedash, and Juha Tuoriniemi. *Studies on Helium Liquids by Vibrating Wires and Quartz Tuning Forks*. Journal of Low Temperature Physics **165**, 132 (2011).

V J. Rysti and J. Tuoriniemi. *Mechanical Oscillators in Inviscid Compressible Fluids*. Journal of Low Temperature Physics **171**, 273 (2013).

VI J. Rysti and J. Tuoriniemi. *Quartz Tuning Forks and Acoustic Phenomena in Superfluid Helium*. arXiv:1304.2795 (2013).

VII Anssi Salmela, Juha Tuoriniemi, Elias Pentti, Alexander Sebedash, and Juho Rysti. *Acoustic resonator providing fixed points of temperature between 0.1 and 2 K*. Journal of Physics: Conference Series **150**, 012040 (2009).

VIII A. Salmela, J. Tuoriniemi, and J. Rysti. *Acoustic Resonances in Helium Fluids Excited by Quartz Tuning Forks*. Journal of Low Temperature Physics **162**, 678 (2011).

IX J Tuoriniemi, J Rysti, A Salmela, and M Manninen. *Mode analysis for a quartz tuning fork coupled to acoustic resonances of fluid in a cylindrical cavity*. Journal of Physics: Conference Series **400**, 012077 (2012).

Throughout the introductory part, the publications will be referred to by their Roman numerals.

Author's contribution

The publications in this Thesis are a result of team work by the YKI group at the O.V. Lounasmaa (Low Temperature) Laboratory.

The author performed the analytical and numerical calculations in publications **I** and **II**, did some data analysis in **II**, wrote publication **I** and first versions of chapters III–V of **II**. He performed the calculations and wrote publication **III**.

In publications **IV**, **VII**, and **VIII**, the author had a lesser role in the preparations of the experiments, discussion of the results, and commenting the manuscripts. He performed the modeling and numerical simulations in **V** and **VI**, and wrote the manuscripts. For publication **IX** the author performed some initial numerical work and contributed to the discussion of the results.

The author participated in the relocation and reconstruction of the group's nuclear demagnetization cryostat, when the laboratory moved into new premises. A specific responsibility assigned to him during most of the Thesis work was to update and expand the computer program, which is used to control and automate experiments and collect data. The author is largely responsible for the yet unpublished work in the Thesis, which will be refined and published later.

Chapter 1

Introduction

I imagine experimental physicists must often look with envy at men like Kamerlingh-Onnes, who discovered a field like low temperature, which seems to be bottomless and in which one can go down and down.

Richard Feynman

The field of low temperature physics truly began, when Heike Kamerlingh Onnes first reached a temperature of 4.2 K and liquefied helium in 1908 [1]. Based on the understanding of physics at the time, nothing spectacular was expected to occur at such low temperatures. Soon thereafter, however, surprising and unexplainable effects were observed. The electrical resistance of mercury, for example, suddenly dropped to zero when cooled with liquid helium. This is a phenomenon known as superconductivity. Later it was observed that liquid helium itself, when cooled to 2.2 K, shows very peculiar properties. It becomes a superfluid, which can flow without friction. Somewhat ironically, helium is one of the most trivial substances at room temperature, since it is chemically inert, but one of the most intriguing substances at low temperatures. Today we understand these interesting effects as arising from quantum mechanics, the counterintuitive, but apparently fundamental, underlying characteristic of our Universe.

Helium has two stable isotopes, the more ordinary ^{4}He, which Kamerlingh Onnes was able to liquefy, and the extremely rare ^{3}He, which must be produced artificially for any macroscopic quantity. At room temperature, the two helium isotopes behave essentially identically, the only difference being in mass. At low temperatures, however, they act very unequally and reveal a fundamental difference of nature. This is because, fortunately for physicists, the two isotopes represent the two fundamental types of particles, ^{3}He behaving like a fermion and ^{4}He a boson. All known particles in the Universe can be divided into these

two classes. To which group a particle belongs, depends on its spin. Integer spin particles are bosons and half-integer spins are fermions. The one unpaired neutron in a ^{3}He nucleus gives the atom an effective spin of 1/2, compared to zero spin of ^{4}He. Helium thus provides us with an opportunity to study fermions and bosons in the quantum mechanical regime in a controlled laboratory environment. The different particle types of helium isotopes do not make a difference in our everyday room-temperature lives, because quantum effects are largely obscured by such high temperatures. As we go down to colder and colder, quantum mechanical effects appear and the difference becomes essential. The reason why helium, in particular, is of such importance is that it is the only substance to remain liquid down to low enough temperatures. This is caused by the lightness of helium atoms, which in turn results in a large zero-point motion, and the weak interactions between helium atoms due to van der Waals forces. Because helium is the only liquid at low enough temperatures, it is also the only observable quantum liquid. All other matter is either solid or extremely sparse gas. Helium can be solidified, but this requires elevated pressures (3.44 MPa for ^{3}He and 2.53 MPa for ^{4}He). Interesting phenomena also exist in solid helium, which can be regarded as a quantum solid.

Helium-3 also becomes a superfluid, but the required temperature at about 2 mK is a thousand times lower than for ^{4}He [2]. This is a reflection of the different quantum statistics obeyed by the two isotopes. Bosonic ^{4}He can directly form a Bose-Einstein type condensate, which is the superfluid state. The fermionic ^{3}He, on the other hand, cannot do this due to the Pauli exclusion principle. It must first form pairs of fermions, known as Cooper pairs, which can then form the condensate. Bardeen, Cooper, and Schrieffer (BCS) developed the microscopic theory of superconductivity in 1957, more than 30 years after the invention of quantum mechanics and 45 years after the discovery of superconductivity by Kamerlingh Onnes [3]. Their theory can be extended to more general Fermi systems, including ^{3}He, and the superfluid state of this fermionic helium is understood to be similar to the BCS state of superconducting electrons. The formation of Cooper pairs requires an attractive interaction between the constituent particles. This is also a sufficient condition. That is, if there is an attraction between fermions, they will form Cooper pairs at low enough temperatures. Electrons in metals, for example, attract each other through lattice vibrations and thereby form Cooper pairs.

A remarkable feature of mixtures of the two helium isotopes is that the solubility of ^{3}He in ^{4}He remains finite down to absolute zero temperature. This opens up the possibility to do experiments with helium mixtures at very low temperatures and also allows, for example, the construction of a dilution refrigerator,

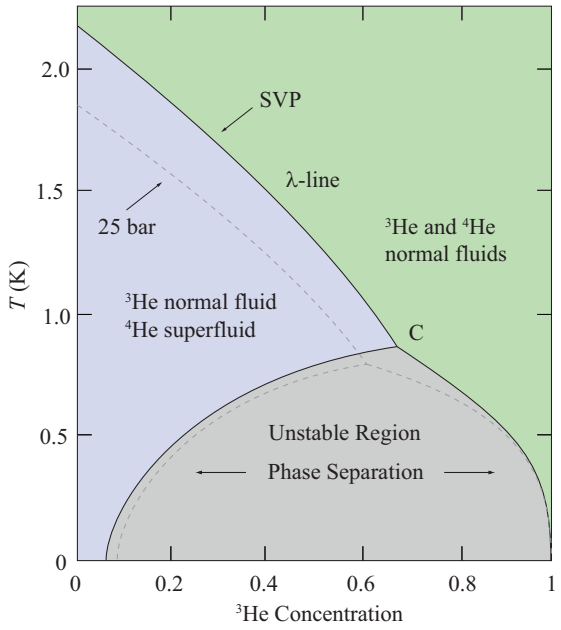

Fig. 1.1 Phase diagram of helium mixtures at the saturated vapor pressure (SVP), which is essentially 0 bar at temperatures below 0.3 K, and at 25 bar. In the green area both isotopes are normal liquids. In the blue area ^{3}He is normal, but ^{4}He is superfluid. The λ-line indicates the ^{4}He superfluid phase transition. The grey area represents an unstable region, where a phase separation occurs into ^{3}He-rich and ^{3}He-dilute phases. The tricritical point is denoted by C. The figure has been created from the data of Ref. 4.

which is the lowest-temperature continuous cooling device invented. Helium mixtures offer a remarkable Fermi system, where the degeneracy temperature and interaction energy can be varied. By changing the concentration, one can study systems from essentially ideal Fermi gas to weakly interacting Fermi liquid. The degeneracy temperature T_F, or Fermi temperature, characterizes the temperature range, where quantum effects become important. For pure ^{3}He one finds $T_F \approx 1$ K. In dilute mixtures at low temperatures it can be varied between zero and approximately 400 mK.

The phase diagram of helium mixtures is given in Fig. 1.1. Below 0.87 K, helium mixtures can separate into two phases, one rich in ^{3}He and the other rich in ^{4}He. The latter is known as dilute ^{3}He–^{4}He mixture. Molar concentration is defined as $x = N_3/(N_3+N_4)$, where N_i is the number of atoms i. At low tempera-

tures the maximum solubility of ^{3}He in ^{4}He is about 6.6% at the saturated vapor pressure (SVP), which is practically zero pressure at low temperatures. The solubility increases at elevated pressures. The ^{3}He-rich phase becomes pure ^{3}He in the zero temperature limit. It is evident from experimental data that an attractive interaction between the ^{3}He atoms dissolved in ^{4}He exists [4, 5]. Therefore, a superfluid state of the ^{3}He component also exists at some low enough temperature. This would be an interesting mixture of Bose and Fermi superfluids. Mixtures have been cooled down to 100 μK with no observation of the superfluid state [6, 7]. Discovering this state has been called the "holy grail of low temperature physics" [8].

Cooling helium to temperatures below 100 μK becomes increasingly more difficult as the thermal boundary resistance between the liquid and the container wall increases rapidly. To achieve lower temperatures, a cooling method, which cools the liquid directly, must be devised. The YKI group of the O.V. Lounasmaa (Low Temperature) Laboratory of Aalto University has been developing a novel cooling method, known as adiabatic melting of solid ^{4}He, to overcome the restriction due to thermal resistance. The method is hoped to provide liquid mixture temperatures well below the current record, low enough to reach the superfluid state of mixtures.

Measuring low temperatures is not an easy task. Helium mixtures can provide useful means to measure temperature, besides being an interesting physical system in itself. The melting curve of helium mixtures could be used as a thermometric standard in a similar manner as pure ^{3}He [9]. Since the ^{3}He component in a helium mixture remains normal fluid to lower temperatures than pure ^{3}He, mixtures have the potential of offering more resolution at temperatures well below 1 mK.

Low temperature helium requires special tools to make observations of its properties. Vibrating objects can be used as probes of liquid helium, since the vibrational characteristics of such resonators depend on the properties of the surrounding medium. Vibrating wires have been traditionally used for this purpose, but in recent years quartz tuning fork resonators, small mechanical oscillators used to keep time, have been found to be well suited as probes in liquid helium [10, 11]. They can be used as thermometers, viscometers, pressure gauges, and density and concentration sensors. The main advantages of quartz tuning forks over vibrating wires are their mass production, and thus low cost, good quality factor, and that they do not require an external magnetic field. The main disadvantage is their more complex geometry, which complicates analysis of their behavior.

A mechanical oscillator, such as a quartz tuning fork, can couple to different sound modes of the surrounding medium. This leads to new phenomena, which can be either a nuisance or be taken advantage of. Ordinary sound, or first sound, is the common traveling density wave of the medium. Superfluid helium can also support other kinds of sound waves. It has become customary to label these modes with ordinal numbers. Zeroth sound is a wavelike change in the shape of the Fermi sphere in ^{3}He. Second sound can be thought of as being a temperature wave, or equivalently an entropy wave. Third and fourth sounds are encountered in restricted geometries.

In this thesis properties of liquid and solid helium mixtures are studied computationally and experimentally. We present both microscopic and macroscopic approaches. The microscopic calculations consider the system at the atomic level. Simulations, which assume a large system from the beginning and experiments can be categorized as macroscopic studies. The results of this thesis revolve around supporting work for the adiabatic melting experiment. In the course of the present studies, some aspects have generated deeper interest in their own right.

Organization of the thesis

This overview of the thesis is organized in the following manner: The adiabatic cooling method and our experimental setup are described in Chapter 2. Interactions between ^{3}He atoms in superfluid ^{4}He, which determine the superfluid transition temperature, are discussed in Chapter 3. These results have been published in **I**. Knowledge of the interactions allows one to compute various other properties, besides the transition temperature, such as solubility, osmotic pressure (**II**), and melting pressure (**III**). Chapter 3 considers such properties of helium. In addition, experimental results for the molar volume of pure ^{3}He are given and simulations using path integral Monte Carlo are presented. Quartz tuning forks are introduced in more detail in Chapter 5 (**IV**). Propagation of different sound modes in helium and their coupling to mechanical oscillators are studied in Chapter 6 (**V**-**IX**). The thesis is summarized and near-future research activities are outlined in the final chapter. Results, which have not yet been published, are presented in sections 4.4, 4.5, and 6.2. These studies will be refined and published later. Material, which is not covered in the accompanying articles, is considered in more detail.

Chapter 2

Refrigeration by Adiabatic Melting

Conventionally helium mixtures have been cooled to low temperatures using adiabatic nuclear demagnetization of copper and coupling the liquid thermally to the nuclear stage via a large surface area, employing sintered metal powder [6, 7]. Achieving liquid temperatures below 100 μK becomes increasingly more difficult, as the thermal boundary resistance grows rapidly at low temperatures. The cooling power decreases and even small heat loads, of the order of picowatts, to the sample prevent reaching lower temperatures.

In some sense, our novel method can be compared to ordinary dilution refrigeration. In a dilution refrigerator, liquid helium mixture exists in the phase separated state. Helium-3 is continuously circulated and ^{3}He atoms are transferred from the rich phase to the diluted phase. This results in cooling, as an amount of energy, the heat of mixing, is absorbed in the process. This is because the enthalpy of ^{3}He is larger in the diluted phase than in the rich phase. An equivalent statement is that entropy per ^{3}He is larger in the mixture than in pure ^{3}He at a given temperature. Exactly the same principle is used in the adiabatic melting refrigeration, except that the isotopes are kept separated in a different way. The separation is achieved by increasing the pressure of the mixture up to the melting pressure and solidifying the ^{4}He component. At low temperatures, the solid is practically pure ^{4}He. As it is melted adiabatically and as reversibly as possible by removing ^{4}He from the cell, the two isotopes mix and cooling occurs. Helium-4 can be transferred to and from the cell selectively using a superleak capillary, through which only superfluid ^{4}He can flow. This is possible, since the crystallization pressure is higher inside the superleak than in bulk. We define the cooling factor by the ratio of initial and final temperatures, $C_\mathrm{F} = T_\mathrm{i}/T_\mathrm{f}$. The adiabatic melting method is not continuous like dilution refrigeration, since the process ends when all solid has been melted.

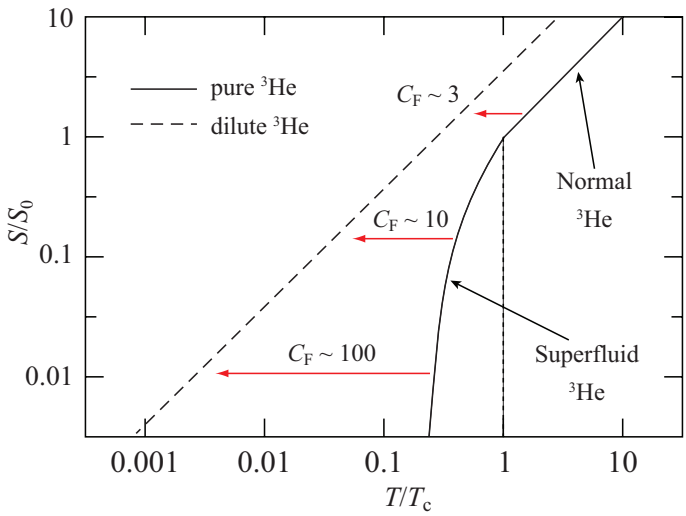

Fig. 2.1 Molar entropies of ^{3}He in the pure and dilute phases as functions of temperature. The arrows indicate adiabatic and reversible transitions from the pure phase to the dilute phase. The resulting cooling factors C_F are indicated. The temperature scale is normalized by the superfluid transition temperature of pure ^{3}He and entropy by the corresponding value of pure ^{3}He.

The relevant entropies are illustrated in Fig. 2.1. At low temperatures ^{4}He, whether liquid or solid, is basically in its ground state and its entropy is negligible in comparison with the ^{3}He component. If the pure ^{3}He is in the normal state when mixing takes place, the situation corresponds to a dilution refrigerator and the cooling factor is approximately $C_F \approx 3$. The crucial point is that the entropy of pure ^{3}He decreases exponentially when it is cooled below its superfluid transition temperature. Thus, the cooling factor also increases considerably, even orders of magnitude. By precooling the pure ^{3}He liquid to a low starting temperature, the adiabatic melting process should result in a very low final temperature for the mixture. The cooling power is determined primarily by the entropy of the dilute phase. Entropy of a degenerate Fermi system S is proportional to the temperature T, and the cooling power $\dot{Q}$ is then

$$\dot{Q} = T\dot{S} \approx (100\ \mathrm{J/mol \cdot K^2})\dot{n}T^2, \tag{2.1}$$

where $\dot{n}$ is the molar rate of ^{3}He transfer between the phases [12]. For a plausible rate of $\dot{n} = 100$ μmol/s and $T = 100$ μK, the cooling power is 100 pW. Since $\dot{Q}$ decreases quickly at low temperatures, all possible heat leaks into the sample

must be eliminated and the melting process must be done as adiabatically and reversibly as possible.

The adiabatic melting method has been proven to work as expected, but due to technical problems in the first experiments, the lowest final temperature was around 300-400 μK [13], [**IV**]. Those results have prompted several improvements to the experimental design, which is shown in Fig. 2.2. The shape of the experimental cell is rather flat to reduce the amount of viscous heating. The superleak in the first experiment did not function properly, which restricted the achievable melting rate of the solid. The superleak in the current design is not operated directly from room temperature, since in the previous experiment apparently some uncontrollable oscillations took place in the capillary. This was likely to occur at the superfluid-normal fluid interface. Therefore, the addition and removal of ^{4}He from the cell will be performed with cold bellows.

During precooling of the pure ^{3}He, thermal contact to the cold cell walls should be good. However, when the adiabatic melting is commenced, the sample should be decoupled from the cell so that cooling power would not be wasted on cooling the cell structures. To have this in control, the sintered metal powder is located in a separate volume, which can be thermally isolated from the cell volume by a "thermal gate", which is essentially a pressure operated cold valve. The experimental setup will be equipped with quartz tuning fork resonators, a noise thermometer, Pt-NMR thermometers, and a capacitive pressure gauge. A nucleator is placed inside the cell to ensure solid nucleation at the proper location.

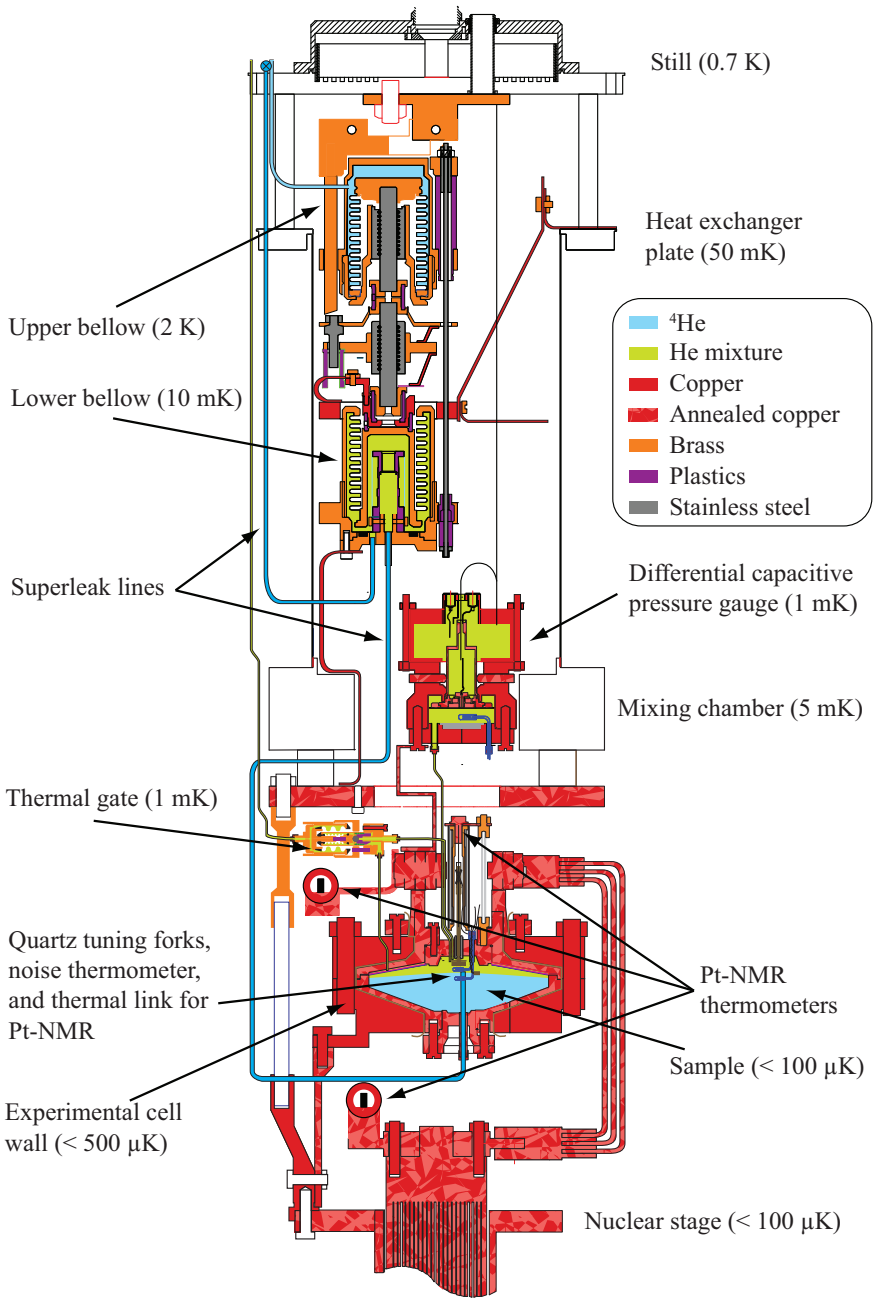

Fig. 2.2 Experimental setup for the adiabatic melting refrigeration.

Chapter 3

Effective Interactions in Helium Mixtures

As a noble gas, helium atoms interact directly only through van der Waals forces. This is weak compared to other elements, allowing helium to remain liquid at low temperatures, but still strong enough to prevent considering the system as essentially free particles. In the spirit of Landau [14, 15], it is useful to not consider the strongly interacting bare atoms, but rather quasiparticles with some effective mass and weak effective interactions. In pure ^{3}He, the effective interaction takes into account the direct interaction, but also indirect effects, such as those arising from spin fluctuations. The attraction required for the superfluid state is caused by the exchange interaction. A quasiparticle with a certain spin orientation causes a local polarization of the neighboring quasiparticles. The tendency for neighboring quasiparticles to align parallel results in an attractive potential, which leads to the Cooper instability. The direct spin-spin interaction between ^{3}He atoms is the dipole-dipole force between spin-1/2 helium-3 nuclei. This effect is very small, and would yield a very low superfluid transition temperature. The Pauli exclusion principle requires that parallel spin particles remain spatially separated, leading to exchange energy. This exchange energy is a much stronger effect, and is the dominant spin-spin interaction in ^{3}He. It tends to favor parallel spins, ferromagnetic alignment. The principle is very similar to the mechanism which produces ferromagnetism in iron, for example. It is also the reason why the Cooper pairs in pure ^{3}He have the nuclear spins aligned parallel. This is contrary to most metallic superconductors, where the electron pairs have antiparallel spins. One may ask why the bare van der Waals interaction is not enough to result in the superfluidity of ^{3}He. Indeed it could cause Cooper pairing, but it turns out that the transition temperature would be much lower than what is observed [16].

When ^{3}He is dissolved into superfluid ^{4}He, the system changes drastically. At low temperatures ^{4}He is in its ground state and thus only acts as a superfluid background, through which the ^{3}He atoms move. Because ^{3}He is an isotopic impurity, the chemical forces between ^{3}He and ^{4}He are identical. The only way for ^{3}He to distinguish other ^{3}He atoms reside in the mass difference and in quantum statistics, which produce a residual interaction. The ability of ^{3}He to polarize other ^{3}He in its vicinity is decreased compared to pure ^{3}He as their density is lower. However, the mass difference between the two isotopes results in a new type of interaction, absent in pure ^{3}He. The smaller mass of ^{3}He causes its zero-point energy to be larger, and thus the volume occupied by the atom to be larger than by ^{4}He. In a sense, then, ^{3}He atoms in helium mixtures behave as bubbles or holes. These bubbles tend to combine to minimize pressure due to ^{4}He. This is the heuristic explanation for the dominant effective interaction between ^{3}He quasiparticles in helium mixtures. In the language of quantum field theory, the interaction is mediated by the exchange of virtual ^{4}He phonons.

It is useful to consider the mutual interactions between quasiparticles in momentum space, *i.e.*, the Fourier transform of the real space potential

$$V(\mathbf{k}) = \int d^3 r e^{-i\mathbf{k}\cdot\mathbf{r}} V(\mathbf{r}). \tag{3.1}$$

Here the potential is written in terms of the wave vector $k = p/\hbar$. Quasiparticle energy can now be written in the Hartree-Fock approximation as [17]

$$\varepsilon(k) = -E_3 + \frac{(\hbar k)^2}{2m^*}\left(1+\gamma k^2\right) + n_3 V(0) - \int \frac{d^3k'}{(2\pi)^3} V(\mathbf{k}-\mathbf{k}') f(k'), \tag{3.2}$$

where E_3 is the binding energy of a single ^{3}He atom in superfluid ^{4}He, m^* is the effective mass of a ^{3}He quasiparticle in the zero concentration limit, the γk^2-term is a small correction to the basic effective mass model of Landau Fermi-liquid theory [18], and n_3 is the ^{3}He particle density. Of the interaction terms, $n_3 V(0)$ is the direct Hartree interaction energy. As can be seen from the Fourier transform, Eq. (3.1), $V(0)$ represents a spatial average of the interaction. The second interaction term in Eq. (3.2) is the exchange energy due to interaction between particles with parallel spin. In the above dispersion relation, $f(k)$ is the Fermi-Dirac distribution function

$$f(k) = \frac{1}{e^{\beta(\varepsilon(k)-\mu)}+1}, \tag{3.3}$$

where $\beta = 1/(k_{\mathrm{B}}T)$, as usual and μ is the chemical potential. The latter is determined by demanding

$$n_3 = 2\int f(k)\frac{d^3k}{(2\pi)^3}. \tag{3.4}$$

In a general case this is solved numerically. A low temperature series expansion can be used at sufficiently low temperatures. The chemical potential is very useful in connecting the interaction potential to many observable quantities.

The idea of mass-difference interaction was developed by Bardeen, Baym, and Pines (BBP) [19]. The excess volume occupied by the ^{3}He atoms is seen in the molar volume of mixtures, v_m, written in the form

$$v_\mathrm{m} = v_{40}(1 + \alpha x), \tag{3.5}$$

where v_{40} is the molar volume of pure ^{4}He, x is the molar ^{3}He concentration, and α is the so-called BBP parameter, or the excess volume parameter. From the mass difference of the two isotopes, one can expect α to be approximately $1/3$. The experimental value at zero pressure is $\alpha \approx 0.28$ and at 2.5 MPa $\alpha \approx 0.17$ [20]. BBP showed that in the long wavelength limit (zero momentum transfer) the mass difference results in an attractive interaction between ^{3}He quasiparticles. They also argued that the momentum dependence of the potential should be quadratic at low momenta.

We have determined the effective interaction potential phenomenologically at all pressures of liquid mixtures by fitting previously measured solubility [21] and osmotic pressure [**II**] data to a chosen functional form for $V(k)$. We used the zero-temperature osmotic pressure and solubility data and the temperature dependence of solubility. The interaction was assumed to be independent of spin. The obtained potential can then be used to calculate many derived properties of helium mixtures. These are discussed in the following section and chapter.

3.1 Predicted superfluid transition

In their original theory of superconductivity, Bardeen, Cooper, and Schrieffer considered pairs of electrons with opposite spins (total spin $S = 0$) and zero orbital angular momentum ($l = 0$) [3]. This is called the s-wave pairing, and it occurs for most metallic superconductors. For pure ^{3}He, only p-wave pairing ($S = l = 1$) is observed, since the attractive interaction is between parallel-spin particles. Because the interaction between fermions in helium mixtures is not primarily dependent on spin, s-wave pairing, and in principle d-wave, f-wave etc., is also possible. The original BCS theory can be generalized to include other possible pairing mechanisms [22, 23]. The transition temperature for a state with orbital angular momentum l is given by

$$T_\mathrm{c} \lesssim T_\mathrm{F} e^{1/N(0)V_l}, \tag{3.6}$$

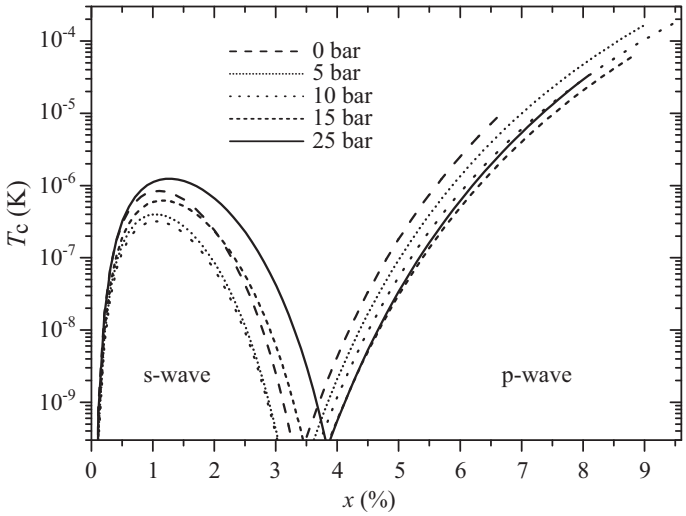

Fig. 3.1 Calculated superfluid transition temperatures of dilute ^{3}He–^{4}He mixtures at various pressures as functions of ^{3}He concentration. The s-wave and p-wave pairing mechanisms are denoted.

where V_l is the order l coefficient of the Legendre polynomial expansion of $V(k)$, T_F is the Fermi temperature, and $N(0)$ is the density of states at the Fermi surface. The factors $N(0)V_l$ can be connected to the Landau parameters, which in the Hartree-Fock approximation are some integrals of $V(k)$ over the momentum space. Since the total wave function of Cooper pairs must be antisymmetric, the spin part of the wave function must be antisymmetric ($S = 0$) for symmetric orbital wave functions (even l), and vice versa. The resulting superfluid transition temperatures for helium mixtures using our effective interaction potential are given in Fig. 3.1 The general shapes of the curves are similar to those obtained by others. The s-wave pairing dominates at low concentrations at all pressures. Above $x \approx 3.5\%$, p-wave pairing becomes preferable. The maximum in the s-wave channel can be understood so that the density of states increases proportionally to $x^{1/3}$, but as concentration, and momentum transfer between the quasiparticles, is increased, the potential reaches a repulsive region for s-wave pairing. The same argument can be applied to p-wave as well, except that the system never reaches a repulsive momentum range within limits of solubility where T_c would begin to decrease. The maximum transition temperature according to our results is $T_\mathrm{c} \approx 200\,\mu$K, which is reached at the maximum concentration at pressures between 5 bar and 10 bar. The transition temperature at 25.3 bar,

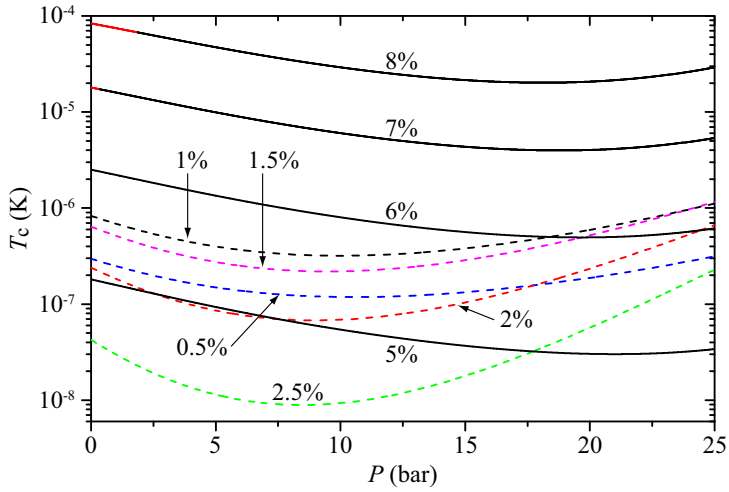

Fig. 3.2 Calculated superfluid transition temperatures of dilute ^{3}He–^{4}He mixtures at various concentrations as functions of pressure. The dashed lines denote s-wave and solid lines p-wave pairing. The red color in the graphs for 7% and 8% mixtures indicate a state of supersaturation.

the operating pressure of the adiabatic melting experiment, is about 40 μK. Our results are optimistic in the sense that estimates by many orders of magnitude lower have been proposed [19, 24–28], and our maximum values are in the region of experimentally achievable temperatures. Higher estimates have also been given by others, some of which have clearly been excluded experimentally [29–32]. Dilute ^{3}He–^{4}He mixtures have been cooled to around 100 μK without any indication of the superfluid transition [6, 13]. We note, however, that the concentration in the experiment of Oh *et al.* at 10 bar pressure was not quite the maximum 9.5%, but instead 9%. Our calculation gives $T_c \approx 100$ μK under these conditions, about the same as the lowest experimentally obtained temperature. We should stress that since the transition temperature has an exponential dependence on the interaction strength, it is quite sensitive to the exact shape of $V(k)$. The observable quantities we have used to determine it, solubility and osmotic pressure, are not so sensitive to the detailed shape. We must allow our calculated T_c to have at least an order of magnitude uncertainty.

Fig. 3.2 shows the transition temperatures plotted as functions of pressure at several concentrations. For low concentrations, only the s-wave channel is given (dashed lines) and for high concentrations, only p-wave (solid lines) is plotted.

The red color in the 7% and 8% data indicate supersaturated states, since the equilibrium concentration is lower than these in the extended pressure ranges. The amount of supersaturation depicted in the 8% data is impossible to achieve, but is shown for curiosity. Usually the pure phase is nucleated at $\sim 0.3\%$ supersaturation at low temperatures.

Chapter 4

Properties of Helium Mixtures

The first three sections of this chapter consider various properties of helium mixtures, which are calculated using the effective interaction potential discussed in the previous chapter. The final two sections present other results.

4.1 Solubility

Saturation solubility of ^{3}He in superfluid ^{4}He is determined from the condition that chemical potential of ^{3}He in the dilute phase equals that in the rich phase. At low temperatures the rich phase is practically pure ^{3}He, so that we find the low temperature solubility from $\mu_3 = \mu_{30}$. Below 500 mK, the solubility of ^{4}He in ^{3}He has been determined experimentally to be approximately [33]

$$x_4 = 0.15(T/\mathrm{K})^{3/2} e^{-0.30\ (\mathrm{K}/T)}. \tag{4.1}$$

Concentration of ^{4}He decreases extremely rapidly below a few hundred millikelvins. In fact, ^{3}He at low temperatures offers undoubtedly the "purest system" available for experiments, if purity is defined as the amount of dissolved impurities in thermodynamic equilibrium.

The Gibbs-Duhem equation $\sum_i N_i d\mu_i = -SdT + VdP$ is useful in obtaining various thermodynamic identities. By integrating this equation, the chemical potential of pure liquid helium-3 is given by

$$\mu_{30}(T,P) = -L_{30} - \int_0^T s_{30} dT' + \int_0^P \frac{v_{30}(0,P')}{N_\mathrm{A}} dP', \tag{4.2}$$

where L_{30} is the latent heat of vaporization per atom, s_{30} is the entropy per ^{3}He atom, v_{30} is the molar volume, and N_A is the Avogadro constant. The chemical

potential of ^{3}He in the mixture phase is determined from Eq. (3.4) or by using the low temperature series expansion [**I**]. We used heat capacity data of Greywall [34] to compute the entropy, and molar volume data of Greywall [35] and Abraham *et al.* [36, 37].

The saturation solubility of ^{3}He in superfluid ^{4}He at low temperatures is often written as

$$x_s = x_0(1+\beta T^2), \tag{4.3}$$

where both x_0 and β depend on pressure. Fig. 4.1 shows the measured and calculated solubilities in the zero temperature limit over the entire pressure range of liquid mixtures. Agreement is very good, which of course is no surprise, since the experimental data were used to find the phenomenological interaction potential in the first place, as was discussed in the previous chapter. The saturation solubility increases from its zero pressure value of approximately 6.7% up to about 9.5% at 10 bar, where it assumes its maximum value, and begins to decrease. At the melting pressure of helium mixtures, solubility is 8.2%. There is more scatter in the experimental data of the temperature coefficient, but overall agreement between experiment and calculation is good.

4.2 Osmotic pressure

Osmosis is a phenomenon encountered in many places in nature. It can occur, when a system is composed of several distinguishable fluid components and a semipermeable barrier, which allows only some of the components to pass through it. A concentration difference over the barrier results in a pressure difference as well, which is called the osmotic pressure π. The definition of osmotic pressure in helium mixtures is visualized in Fig. 4.2. Two vessels are connected by a superleak, which allows only superfluid, in this case ^{4}He, to flow through it. Superfluid will flow until the chemical potentials of ^{4}He are equal on both sides, at which point a pressure difference between the two sides exists. The effect of ^{3}He on ^{4}He on one side is balanced by an increase in pressure on the other. Thus, the condition of equilibrium is

$$\mu_4(T,P,x) = \mu_{40}(T,P-\pi). \tag{4.4}$$

Using the Gibbs-Duhem equation, we can determine the change in the chemical potential of ^{4}He due to added ^{3}He. It is given by [**II**]

$$\delta\mu_4 = \frac{x}{x-1}\mu_3(x) + \int_0^x \frac{1-\xi^2\alpha'(\xi)}{(\xi-1)^2}\mu_3(\xi)d\xi, \tag{4.5}$$

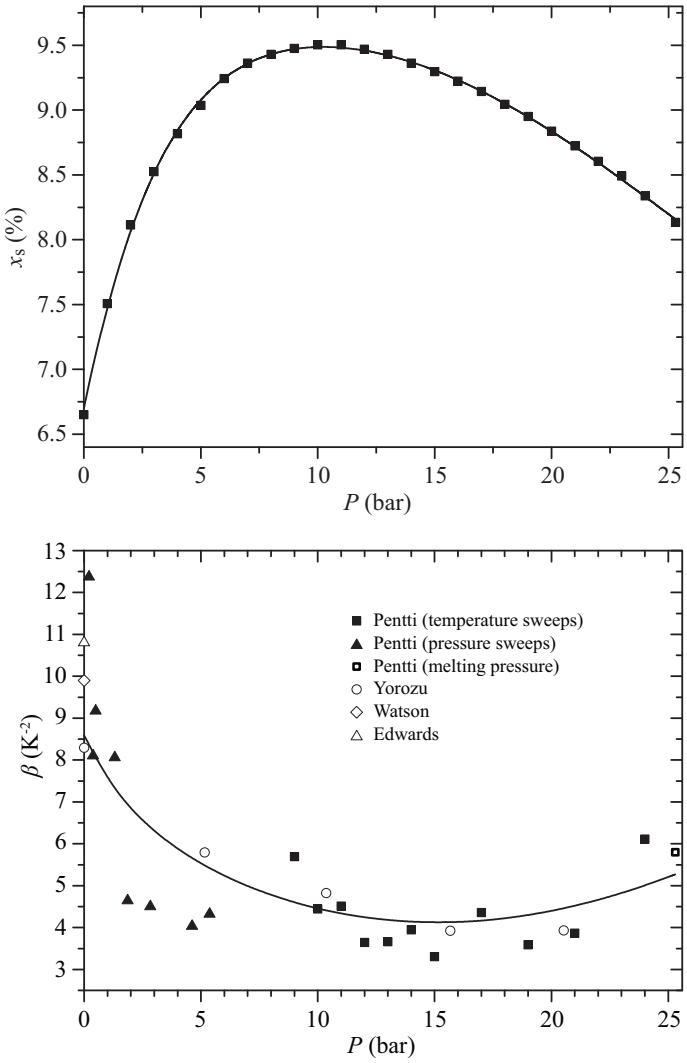

Fig. 4.1 Measured and calculated saturation solubility of ^{3}He in superfluid ^{4}He over the entire pressure range of liquid mixtures. The upper image shows the zero-temperature solubility and the lower image its quadratic temperature coefficient β from Eq. (4.3). Experimental data are from Pentti *et al.* [21], Yorozu *et al.* [25], Edwards *et al.* [38] and Watson *et al.* [20].

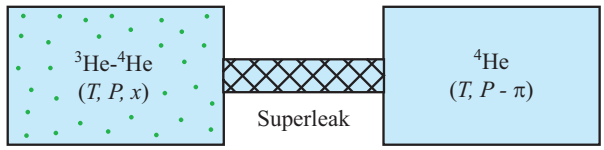

Fig. 4.2 Definition of osmotic pressure π of dilute ^{3}He–^{4}He mixtures. The two vessels are connected by a superleak, which is permeable only to the superfluid ^{4}He. A pressure difference, the osmotic pressure, develops between the vessels. Temperature is the same on both sides.

where a small effect of the concentration dependence of α (BBP parameter) is also taken into account. The chemical potential of ^{3}He is obtained from Eq. (3.4). With the aid of a Maxwell relation, this chemical potential difference can be connected to the osmotic pressure as

$$\pi = -n_{40}\delta\mu_4, \tag{4.6}$$

where n_{40} is the particle density of pure ^{4}He.

We measured the difference between the crystallization pressures of pure ^{4}He and dilute ^{3}He–^{4}He mixtures at various concentrations and temperatures. The melting pressure difference $\Delta P_{\rm m}$ is related to the osmotic pressure through [**II**]

$$\pi = \frac{v_{40}^{\rm L} - v_{40}^{\rm S}}{v_{40}^{\rm L}}\Delta P_{\rm m} \approx 0.095 \cdot \Delta P_{\rm m}, \tag{4.7}$$

where the molar volumes of pure ^{4}He in the liquid and solid phases are indicated. The temperature dependence of the osmotic pressure as a function of concentration can be used to estimate the (concentration independent) effective mass of a ^{3}He quasiparticle in superfluid ^{4}He, since the temperature coefficient is primarily determined by the effective mass and is only weakly dependent on the ^{3}He-^{3}He interactions. Before determining the interaction potential we found the effective mass by assuming non-interacting ^{3}He quasiparticles and taking the interactions into account in an approximate manner. The result of our fit at 2.53 MPa pressure is $m^* = 2.91m_3$, which is in agreement with effective masses obtained by others at lower pressures [39–43]. The measured and calculated osmotic pressures are given in Fig. 4.3. Calculations for both interacting and non-interacting ^{3}He are given for comparison.

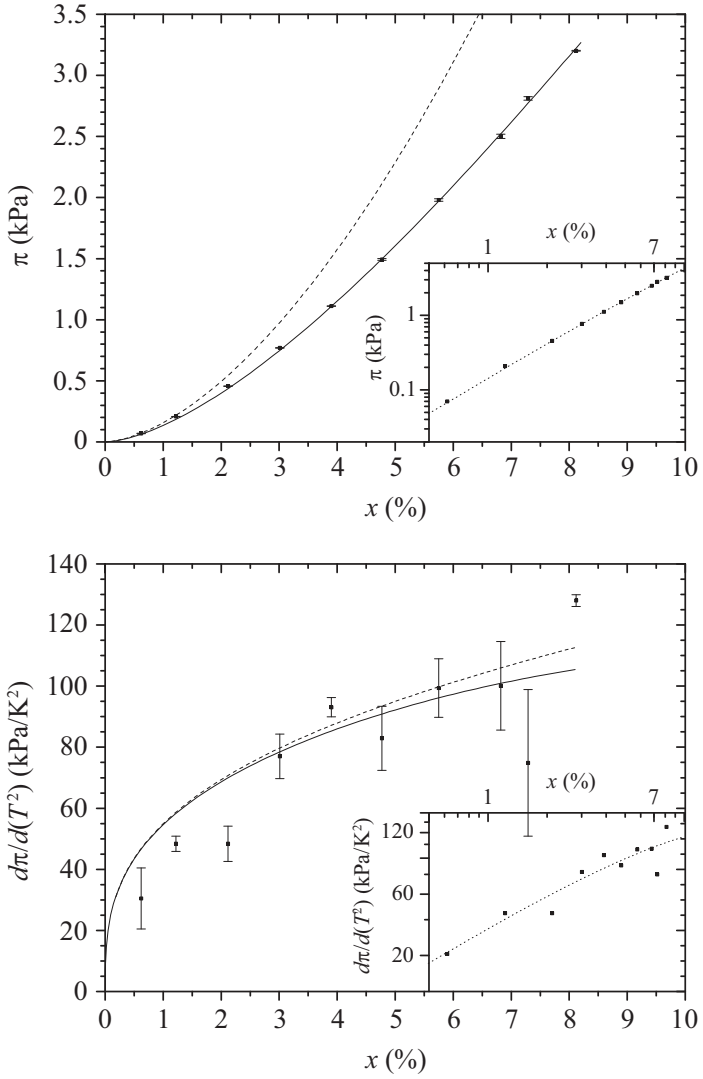

Fig. 4.3 The zero temperature osmotic pressure (upper figure) and its low temperature quadratic temperature coefficient (lower figure). The dots with error bars are the experimental data, the solid lines are the calculated values including interactions between ^{3}He, and the dashed lines are the calculated results assuming non-interacting ^{3}He quasiparticles. The inserts show the same data on logarithmic scales together with semiempirical fits.

4.3 Melting pressure

Solubility saturated helium mixture at the melting pressure consists of one or two liquid phases and one or two solid phases. At low temperatures solid helium mixture can experience a phase separation to ^{3}He-rich and ^{3}He-dilute phases similarly as a liquid mixture. For three simultaneous phases the system is univariant, whose properties depend uniquely on temperature. Four coexisting phases correspond to a quadruple point in the phase diagram. Below the tricritical point, the saturated system is always univariant.

The slope of the melting curve (or in general the coexistence curve of any two phases) is determined by the Clausius-Clapeyron relation

$$\frac{dP}{dT} = \frac{\Delta s}{\Delta v}, \tag{4.8}$$

where Δs is the molar entropy difference and Δv the molar volume difference between the two phases. At low temperatures, the entropy difference essentially determines the shape of the melting curve of helium, since the molar volumes do not change much. Because the ^{3}He component of liquid helium mixtures remains normal to lower temperatures than pure ^{3}He, its entropy remains larger, and thus mixtures have the potential to offer superior resolution at low temperatures compared to pure ^{3}He if used as a thermometric standard. The provisional low temperature scale from 0.9 mK to 1 K (PLTS-2000) uses the melting pressure of ^{3}He to define the scale [9].

Below 0.5 K, phonon related effects can be neglected and thus all properties of ^{4}He, whether liquid or solid, can be regarded independent of temperature. The entropy of cold ^{4}He is negligible compared to ^{3}He and the solid phase is essentially pure ^{4}He. Therefore ^{3}He in the liquid phases determine the melting pressure. The entropy of a Fermi system increases quadratically as a function of temperature at low temperatures. For these reasons, the melting pressure of helium mixtures increases proportional to T^2. As temperature increases, ^{3}He begins to dissolve into the solid. This turns the melting pressure down. The maximum pressure is obtained at around 300 mK. At about 400 mK, the pressure equals that of pure ^{4}He. A minimum is reached at approximately 1 K, after which a positive slope is observed again. The preferable crystal structure changes from hexagonal close-packed (hcp) of pure ^{4}He to body-centered cubic (bcc) of pure ^{3}He during increasing concentration of the solid phase.

To find the equilibrium state, we need the chemical potentials of both ^{3}He and ^{4}He in each of the phases. Since we are considering a saturated mixture at low temperature, we have three phases, and subsequently four equations of the form

$\mu^A_{3,4} - \mu^B_{3,4} = 0$, where A and B denote two different phases. The four variables, which are solved from this group of nonlinear equations at a given temperature, are the melting pressure P_m and the concentrations x^D, x^R, and x^S. The superscripts D, R, and S refer to the ^{3}He-dilute liquid, ^{3}He-rich liquid, and the solid, respectively. We also denote hcp as h, bcc as b, and liquid as L. At temperatures above 10 mK, ordering of the nuclear spins in solid ^{3}He and the superfluid transition of pure ^{3}He liquid can be neglected. The magnetic ordering temperature of pure solid ^{3}He is $T_N = 0.9$ mK. In the following subsections, all the required chemical potentials in the different phases are discussed. A similar calculation has been presented by Edwards and Balibar [44], but we have the benefit of some more recent experimental data and more accurate description of the ^{3}He-^{3}He interactions.

4.3.1 ^{3}He-dilute liquid

The chemical potentials of the dilute liquid phase were already discussed in the previous sections. For ^{3}He it is given by numerical solution of Eq. (3.4). The chemical potential of ^{4}He is

$$\mu_4^D = \mu_{40}^L + \delta\mu_4^D, \tag{4.9}$$

where $\delta\mu_4^D$ is given by Eq. (4.5).

4.3.2 ^{3}He-rich liquid

The rich phase is almost pure ^{3}He, so the chemical potential of ^{3}He in the liquid can be approximated by

$$\mu_3^R = \mu_{30}^L + k_B T \ln x^R, \tag{4.10}$$

where μ_{30}^L, the chemical potential of pure ^{3}He liquid, is given by Eq. (4.2) and $x^R \approx 1$ is the concentration of ^{3}He in this phase. Since $x^R > 0.98$ below 0.5 K, we can use the Maxwell-Boltzmann statistics to obtain the chemical potential of ^{4}He:

$$\mu_4^R = \mu_{40}^L + \Delta E_4 + k_B T \ln\left[\left(\frac{T_4^*}{T}\right)^{3/2}(1 - x^R)\right] \tag{4.11}$$

The chemical potential of pure liquid ^{4}He, μ_{40}^L, is not actually needed, since it cancels with the same term contained in μ_4^D and it is written in terms of μ_4^S, when compared to the solid phase. In the above equation ΔE_4 is the difference between one ^{4}He atom in ^{3}He versus in ^{4}He. It is given by

$$\Delta E_4 = \Delta E_4^0 - \int_0^P \left[v_{40} - (1 + \alpha_4^0)v_{30}\right] dP'. \tag{4.12}$$

Edwards *et al.* found $\Delta E_4^0 = 0.21$ K [45]. We have used the values for $\Delta E_4(P)$ given by He *et al.*[46]. The factor α_4^0 is the zero-temperature value of the equivalent parameter in rich ^{3}He as the BBP parameter in dilute ^{3}He in Eq. (3.5). Its value is obtained from [45]. The characteristic temperature T_4^* is

$$T_4^* \equiv \frac{2\pi\hbar^2}{m_4^* k_B}\left(\frac{N_A}{v_{30}}\right)^{2/3}, \tag{4.13}$$

where m_4^* is the effective mass of one ^{4}He in ^{3}He. Laheurte found to his experimental accuracy that $m_4^* \propto v^{-2/3}$ [47]. Thus, T_4^* is constant over pressure. Edwards and Balibar used a value $T_4^* = 1.114$ K. Later measurements indicate, however, that the effective mass of ^{4}He in ^{3}He is significantly smaller than the value used by them. Edwards *et al.* found $m_4^* = 1.1 m_4$ and $T_4^* = 4.91$ K [45] instead of the earlier value $m_4^* \sim 4.5 m_4$ [47, 48]. The smaller value was later supported by a microscopic calculation, which found $m_4^* = 1.21 m_4$ [49]. We used in our calculations the experimental value $m_4^* = 1.29 m_4$ [46] and thus $T_4^* = 4.19$ K.

When comparing the chemical potentials in the liquid and solid phases, it is convenient to write pure ^{3}He in the form

$$\mu_{30}^{L} = \mu_{30}^{b} + \int_{P_{30}^{m}(T)}^{P} \left[v_{30}^{L}(T,P') - v_{30}^{b}(T,P') \right] dP', \tag{4.14}$$

Where P_{30}^{m} is the melting pressure of pure ^{3}He [9]. The same applies for ^{4}He. We used the molar volume data for the two isotopes from Grilly [50, 51], Driessen *et al.* [52], Halperin *et al.* [53], and Scribner *et al.* [54].

4.3.3 Solid phase

The regular solution model has been shown to reproduce experimental results in solid helium mixtures with good accuracy [44, 55]. This model relates the Gibbs free energy of a mixture to the free energies of the pure substances. The atomic arrangement is assumed to be completely random and the ideal solution model is simply supplemented by an "excess free energy" term. The Gibbs free energy per atom in the mixture $g(T,P,x) \equiv G/N$ is related to the free energies of the pure substances by

$$g(T,P,x) = x g_3(T,P) + (1-x) g_4(T,P) + T S_m(x) + g_E(T,P,x), \tag{4.15}$$

where S_m is the entropy of mixing of an ideal solution

$$S_m(x) = k_B \left[x \ln x + (1-x)\ln(1-x) \right] \tag{4.16}$$

In the regular solution model the excess free energy is assumed to be of a simple form

$$g_{\mathrm{E}}(T,P,x) = A(P)x(1-x), \tag{4.17}$$

with some pressure-dependent factor A. This cannot be directly applied to situations, where the pure systems have different crystal structures, because it is a continuous function of x. We can, however, write the excess energy separately for both crystals

$$\begin{aligned} g_{\mathrm{E}}^{\mathrm{h}}(T,P,x) &= A^{\mathrm{h}}(P)x(1-x) + x\Delta_3(T,P) \\ g_{\mathrm{E}}^{\mathrm{b}}(T,P,x) &= A^{\mathrm{b}}(P)x(1-x) + (1-x)\Delta_4(T,P), \end{aligned} \tag{4.18}$$

where $\Delta_3 \equiv g_3^{\mathrm{h}} - g_3^{\mathrm{b}}$ is the free energy difference between pure hcp and bcc ^{3}He. Similarly for Δ_4 between bcc and hcp. Edwards and Balibar found that A^{h} and A^{b} are very close to one another, and a single factor A suffices [44]. The chemical potential is found from the Gibbs energy by $\mu_i = \partial G/\partial N_i$. The result for solid ^{3}He is

$$\mu_3^{\mathrm{b(h)}} = \mu_{30}^{\mathrm{b}} + A(1-x^{\mathrm{S}})^2 + k_{\mathrm{B}}T\ln x^{\mathrm{S}}\ (+\Delta_3)\,, \tag{4.19}$$

where Δ_3 is omitted in the bcc phase and included in the hcp phase. Similarly for ^{4}He we have

$$\mu_4^{\mathrm{h(b)}} = \mu_{40}^{\mathrm{h}} + A(x^{\mathrm{S}})^2 + k_{\mathrm{B}}T\ln(1-x^{\mathrm{S}})\ (+\Delta_4)\,, \tag{4.20}$$

where Δ_4 is omitted in the hcp and included in the bcc phase. We used the values for A, Δ_3, and Δ_4 from Ref. 44.

4.3.4 Results

We solved the melting curve and the concentrations for the two crystal structures separately over the entire temperature range in question (10 mK … 500 mK). The results are shown in Fig. 4.4. As the melting curves for hcp and bcc intersect ($T = 280$ mK, $P = 2.63$ MPa), it becomes energetically favorable to change the crystal structure. The intersection forms a quadruple point, where four phases (hcp, bcc, dilute, rich) coexist. This result agrees well with both Edwards and Balibar [44] ($T = 283$ mK, $P = 2.63$ MPa) and the measurements of Lopatik [56] ($T = 0.28$ K, $P = 2.63$ MPa), and van den Brandt *et al.* [57] ($T = 0.30$ K, $P = 2.63$ MPa). Tedrow and Lee concluded from their experiments that this quadruple point is at $T = 0.37$ K and $P = 2.63$ MPa [58].

According to our calculation, another quadruple point (dilute bcc, rich bcc, dilute liquid, rich liquid) exists at $T = 380$ mK and $P = 2.52$ MPa. In Fig. 4.4 this is seen in the lower plot as a discontinuity in the concentration in the bcc

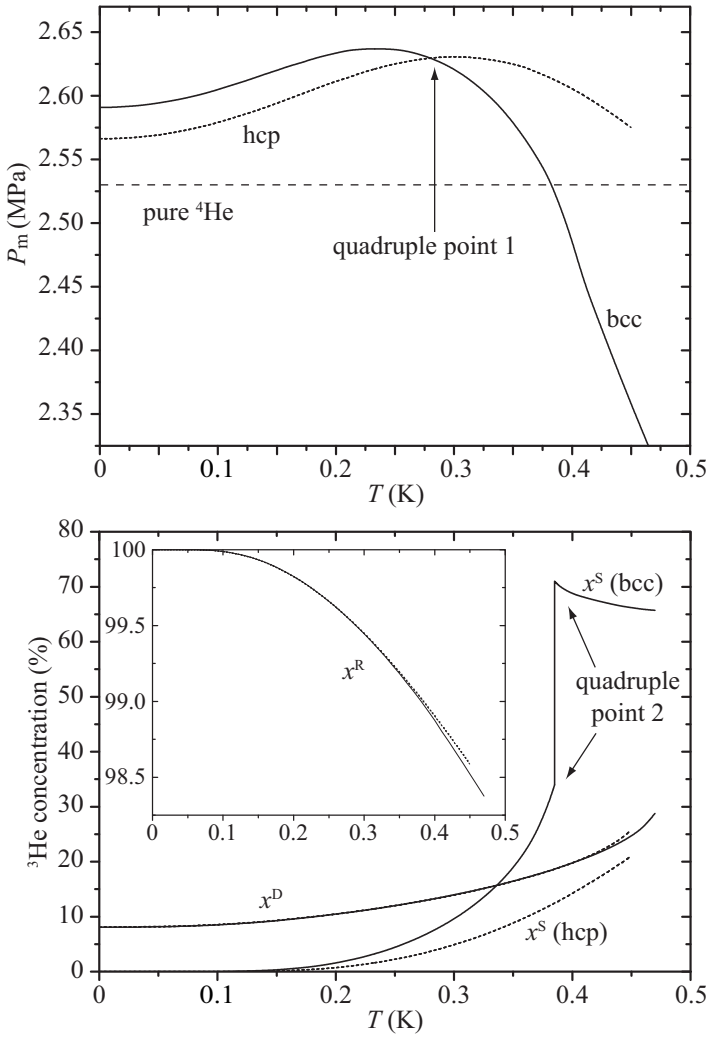

Fig. 4.4 Calculated melting pressure of a saturated helium mixture (top) and the corresponding concentrations of the various phases (bottom). Calculations have been performed separately for the hcp and bcc phases. The melting pressure of pure ^{4}He is also given for reference. Superscripts D, R, and S indicate the ^{3}He dilute, ^{3}He rich, and solid phases, respectively. The concentration x^R is given in the insert to show its small change over the range of temperatures. The quadruple point 1 consists of hcp, bcc, dilute liquid, and rich liquid phases. The second quadruple point is indicated by a jump in the concentration x^S, and includes dilute and rich bcc and liquid phases.

phase x^S. This is contrary to the calculations of Edwards and Balibar, who suggest that the quadruple point does not quite exist [44]. Vvedenskii found in his experiments that it does exist at $T = 380$ mK and $P = 2.60$ MPa [59]. Tedrow and Lee observed a pressure drop and warming at $T = 0.25$ K when cooling, which was attributed to supercooling of the system. On warming they had a kink in pressure and brief cooling at $T = 0.37$ K. We are preparing measurements on the melting curve of helium mixtures, where we intend, among other things, to investigate the hcp-bcc crystal structure transition and the possible quadruple point at around $T = 380$ mK.

4.4 Density of pure ^{3}He

In preparation for experiments on the melting pressure, as discussed above, to investigate some aspects of solubility, and to re-examine the pressure dependence of density of helium mixtures, which are already under way, we have measured the molar volume of pure ^{3}He over the entire pressure range of liquid helium at a low temperature. This has been done in order to calibrate two interdigital capacitors (IDC), which can be used for detecting the density of surrounding helium. These capacitors were originally designed to excite and detect crystallization waves in ^{3}He [60]. Since we used ^{3}He for calibration, we weren't able to measure the absolute value of the molar volume, but rather the relative density over the entire pressure range. Temperature was monitored primarily with a carbon resistor thermometer, and the system was kept at a constant temperature of about 6 mK, 300 mK, or 600 mK. A capacitive pressure gauge was used to measure pressure in the experimental cell. It was calibrated against a room temperature mechanical pressure gauge.

The interdigital capacitors were patterned by a 15 nm layer of chrome and a 50 nm layer of aluminum on high purity crystalline sapphire (Al_2O_3) substrate. The digit spacing and width of the digits were 5 μm with a length of 4.6 mm. The total effective capacitor area was 4.6 mm by 7.4 mm with 740 digits. The capacitors were glued to a copper grid with Stycast 1266 epoxy and attached to the cell walls of a cubic enclosure. In the limit of large number of digits, the capacitance of an IDC can be calculated from

$$C_{\mathrm{IDC}} \approx N\varepsilon_0 l \frac{\varepsilon + \varepsilon_s}{2}, \tag{4.21}$$

where N is the number of digits, ε_0 is the vacuum permittivity, l is the length of the digits, ε is the relative dielectric constant of the medium in contact with the surface, and ε_s is the relative dielectric constant of sapphire. The dielectric

constant of sapphire is $\varepsilon_s \approx 10$, so that the above equation gives a vacuum capacitance of $C_{IDC} \approx 150$ pF. The measured values were 146.22 pF and 155.95 pF for the two units. From Eq. (4.21) we see that the IDC can be used to measure the dielectric constant of the helium sample, which, according to the Clausius-Mossotti relation, is related to the molar volume v by

$$\frac{\varepsilon - 1}{\varepsilon + 2} = \frac{4\pi\alpha_m}{3v}. \tag{4.22}$$

Here α_m is the molar polarizability of helium, whose value and density dependence are obtained from literature [61].

The density measurements were performed when the cell had been filled with ^{3}He to the melting pressure and we began to remove it slowly. The removal was performed gently enough to ensure constant temperature and uniform pressure in the cell. The capacitances were recorded throughout the process. The cell was thermally connected to a dilution refrigerator and temperature was kept constant with a heater using a PID controller. The removal of helium was halted approximately every 100 kPa and pressures were allowed to equalize between the cryostat and a mechanical pressure gauge at room temperature. This provided a calibration for the capacitive pressure gauge. To reduce noise in the data, the IDC and pressure gauge data were smoothed by averaging five adjacent points. The capacitances were fitted to experimental data of the molar volume by other authors using Eqs. (4.21) and (4.22) treating $N\varepsilon_0 l$ and ε_s for the two capacitors as fit parameters. The resulting molar volume curve and the used fit data are shown in Fig. 4.5. The insert shows the difference between our data and the fit data in more detail. Our data have been extrapolated from 3.364 Mpa to 3.433 MPa and from 14.1 kPa to zero pressure. As reference data we have used results from Abraham *et al.* [36] extrapolated to zero temperature, Greywall's data [34, 35] at 5 mK, Halperin *et al.* [53] at the melting curve at temperatures between 3 mK and 20 mK, Grilly [50] at the melting curve at 20 mK, and Scribner *et al.* [54] at the melting curve extrapolated to 20 mK. We performed similar fitting procedure for both capacitors. The difference between the two is shown in the insert as a red curve.

Our results are consistent with previous experiments, considering the scatter in the available data. Some discrepancy in the previous molar volumes at the melting pressure and below it was observed, which manifested itself as a difficulty in fitting a smooth continuous curve to them. Neglecting clearly random effects, the molar volumes obtained by the two capacitors differ less than 0.04% of one another over the entire pressure range. The small systematic difference seen in Fig. 4.5 is a real effect, since plotting the capacitance of one capacitor as a function of the other is not completely linear. The difference is of the order of 0.5 fF

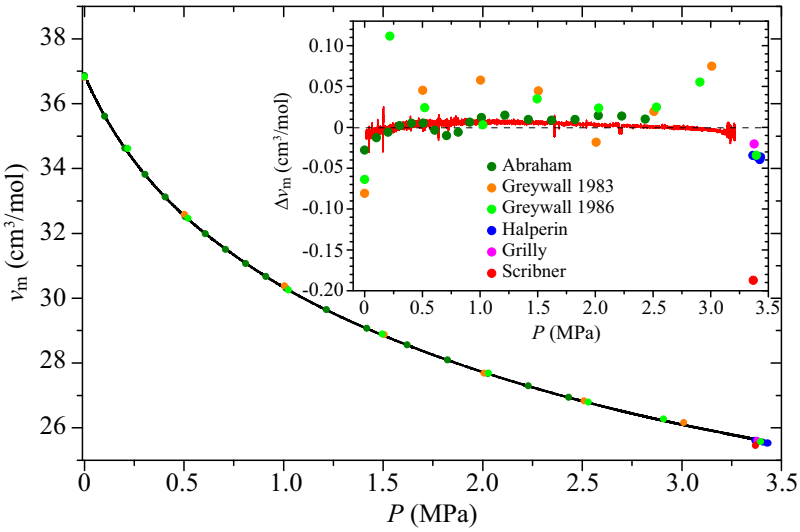

Fig. 4.5 Molar volume of pure ^{3}He. The black line shows our experimental points, when fitted to the data of Abraham *et al.* [36], Greywall [34, 35], Halperin *et al.* [53], Grilly [50], and Scribner *et al.* [54]. The insert shows the difference, when our data are subtracted from the fit data. The red curve is for the molar volume obtained with the other IDC after fitting to the same set of data.

($\sim$ 4 ppm). This effect was reproduced at 300 mK during a re-pressurization of the cell nearly half year later. As of now the origin of this effect is not understood.

The obtained fit parameters are $N\varepsilon_0 l = 25.98$ pF and $\varepsilon_s = 10.26$ for the first capacitor and $N\varepsilon_0 l = 28.44$ pF and $\varepsilon_s = 9.991$ for the other. The difference in the first fit parameter can be attributed to different actual geometries of the two capacitors. The dielectric constant of sapphire for the two should be the same, as they were fabricated on the same singe-crystal sapphire plate oriented in the same direction. We can only speculate that the strain caused by different coefficient of thermal expansion of Stycast compared to sapphire may have deformed the capacitors upon cooling to some degree, causing ε_s to deviate. This is supported by our measurements of surface acoustic waves on the sapphire plates, which exhibited slightly differing resonant characteristics for the two capacitors.

We also performed temperature sweeps from the few millikelvin regime up to few hundred millikelvin. The first capacitor displayed some anomalous behav-

ior in the temperature range of 10 mK, indicating decrease in the molar volume much faster than the expected quadratic. The other capacitor showed a decrease in the molar volume approximately quadratic, but the temperature coefficients were noticeably smaller (about a factor of two) than the ones obtained by others. There are apparently some temperature dependent effects related to the capacitors themselves even at such low temperatures, because compatible effects were observed when the cell was empty. The origin of this issue remains unknown.

4.5 First principles simulations

In this section we report some results of work in progress. Instead of a phenomenological method used in the preceding sections, we now consider a more *ab initio* approach for determining the properties of helium mixtures. The method is based on an alternative formulation of quantum mechanics by Richard Feynman, who also formulated quantum statistical mechanics in terms of the path integral [62]. This concept is well-suited for Monte Carlo methods and the combination of the two is called path integral Monte Carlo (PIMC). In principle, the PIMC method is exact in the sense that errors can be arbitrarily reduced. In practice some approximative schemes must be implemented due to limited computing power.

4.5.1 Path integral Monte Carlo method

Here we briefly outline the idea of PIMC simulations. A system in thermodynamic equilibrium is described by the thermal density matrix, which represents the system in a mixed quantum state with each energy state weighed by the corresponding Boltzmann factor. The density matrix is given by [62, 63]

$$\rho = \sum_i e^{-\beta E_i} |\Psi_i\rangle\langle\Psi_i| = e^{-\beta \hat{H}}, \tag{4.23}$$

where Ψ_i are the eigenfunctions of the Hamiltonian $\hat{H}$ with eigenvalues E_i and $\beta = 1/k_{\mathrm{B}}T$. In numerical simulations it is useful to work in the position representation, because then all the matrix elements of the density matrix are non-negative. We consider a system of N particles in three dimensions. The set of $3N$ coordinates are denoted $\mathbf{R} = \{\mathbf{r}_1, \ldots, \mathbf{r}_N\}$. The density matrix in coordinate representation assumes a form

$$\rho(\mathbf{R}, \mathbf{R}'; \beta) = \langle \mathbf{R}|\rho|\mathbf{R}'\rangle = \sum_i \psi_i^*(\mathbf{R})\psi_i(\mathbf{R}')e^{-\beta E_i}. \tag{4.24}$$

The expectation value of an operator $\hat{O}$ in thermal equilibrium is given by

$$\langle \hat{O} \rangle = Z^{-1} \sum_i \langle \Psi_i | \hat{O} | \Psi_i \rangle e^{-\beta E_i}, \tag{4.25}$$

where the partition function Z is defined as

$$Z = \sum_i e^{-\beta E_i}. \tag{4.26}$$

The expectation value can be written in terms of the position density matrix as

$$\langle \hat{O} \rangle = Z^{-1} \int d\mathbf{R} d\mathbf{R}' \rho(\mathbf{R}, \mathbf{R}'; \beta) \langle \mathbf{R} | \hat{O} | \mathbf{R}' \rangle, \tag{4.27}$$

where the partition function is now

$$Z = \int d\mathbf{R} \rho(\mathbf{R}, \mathbf{R}; \beta). \tag{4.28}$$

Many important operators are diagonal in configuration space and the expectation value becomes

$$\langle \hat{O} \rangle = Z^{-1} \int d\mathbf{R} \rho(\mathbf{R}, \mathbf{R}; \beta) O(\mathbf{R}). \tag{4.29}$$

We can stochastically generate a set of configurations $\{\mathbf{R}_i\}$, which is statistically sampled from a probability density proportional to $\rho(\mathbf{R}, \mathbf{R}; \beta)$. The expectation value $\langle \hat{O} \rangle$ can then be determined by averaging over the set $\{O(\mathbf{R}_i)\}$.

The problem is we don't know the form of $\rho(\mathbf{R}, \mathbf{R}; \beta)$. This is where the path integral method becomes handy. It allows us to calculate the density matrix at low temperatures using a density matrix at high temperatures, where good approximations can be made. This is seen from the fact that the product of two density matrices is a density matrix:

$$e^{-(\beta_1+\beta_2)\hat{H}} = e^{-\beta_1 \hat{H}} e^{-\beta_2 \hat{H}}. \tag{4.30}$$

In position space the above means

$$\rho(\mathbf{R}_1, \mathbf{R}_3; \beta_1 + \beta_2) = \int d\mathbf{R}_2 \rho(\mathbf{R}_1, \mathbf{R}_2; \beta_1) \rho(\mathbf{R}_2, \mathbf{R}_3; \beta_2). \tag{4.31}$$

We can continue this process of division and we see that the temperature at which the density matrix is needed, increases. By dividing the density matrix to $M-1$ parts with equal temperatures, the density matrix in the position space is

$$\begin{aligned} \rho(\mathbf{R}_0, \mathbf{R}_M; \beta) = \int \cdots \int d\mathbf{R}_1 d\mathbf{R}_2 \cdots d\mathbf{R}_{M-1} \times \\ \times \rho(\mathbf{R}_0, \mathbf{R}_1; \tau) \rho(\mathbf{R}_1, \mathbf{R}_2; \tau) \cdots \rho(\mathbf{R}_{M-1}, \mathbf{R}_M; \tau), \end{aligned} \tag{4.32}$$

where $\tau \equiv \beta/M$ is the equivalent of a time step. The large number of integrals we get can be computed together with the Monte Carlo procedure mentioned for the expectation value $\langle \hat{O} \rangle$.

By dividing the density matrix in many parts, we have many configurations of the system at different moments in imaginary time $n\tau$, where n is an integer. A particle can be thought to evolve in imaginary time with steps τ. There is no real dynamics, since we consider the system in thermodynamic equilibrium. The path is the sequence of configurations $\{\mathbf{R}_0, \mathbf{R}_1, \ldots, \mathbf{R}_M\}$ in this "time". In a sense the particles are described by chains of beads connected by springs. Classically this resembles a polymer, which in the diagonal case, $\mathbf{R}_0 = \mathbf{R}_M$, forms a closed ring. Each particle at a given imaginary time interacts only with the other particles at the same "moment in time" (at the same time slice). A particle is connected to itself in successive time steps. Sampling proceeds generally in the following manner: some number of beads of a particle are randomly displaced. After the random displacement, the density matrix of the new configuration is computed and either accepted of rejected by comparing it to the old one by the Metropolis algorithm. Accepted and rejected moves contribute equally to the thermal averages.

For a quantum mechanical many-particle system, one also needs to consider the role of identical particles. Fermions have totally antisymmetric wave functions and bosons have symmetric ones. The density matrix must take into account the exchange of particles, when simulations in the quantum regime are performed. The density matrix for a boson (B) or a fermion (F) system in terms of distinguishable-particle density matrix can be written as

$$\rho_{\mathrm{B/F}}(\mathbf{R}, \mathbf{R}'; \beta) = \frac{1}{N!} \sum_P (\pm 1)^P \rho(\mathbf{R}, P\mathbf{R}'; \beta), \tag{4.33}$$

where P denotes any permutation of the coordinates. Plus sign in the sum are for bosons and minus sign for fermions. In the "ring polymer" analogy, permutations allow the polymers to permute at some time slice with each other, forming larger chains. In boson systems macroscopic chains are understood to indicate a superfluid state. Permutations are not summed over explicitly, since it would be a formidable task even for a relatively small number of particles, but are included in the Monte Carlo step. For bosons this is no problem, since all the permutation terms are positive. For fermions, however, the situation is quite different, as there is cancelation between terms of even and odd permutations. This effectively prevents the use of Monte Carlo evaluation of the integrals. Similar problem arises in other numerical methods as well, and is known as the fermion sign problem. An approximate method, known as the restricted path integral

Monte Carlo (RPIMC) has been developed to a remedy [64]. In this method, paths which change the sign of the density matrix are rejected, and thus only positive contributions are included. One uses a trial density matrix, for example that for free fermions, to estimate, which paths are sign-changing. RPIMC is expected to be relatively accurate for dilute systems. We have not yet performed this type of simulations.

Helium is well described by a Hamiltonian, where the atoms interact by a pair potential $v(r)$:

$$\hat{H} = -\frac{\hbar^2}{2m}\sum_{i=1}^{N}\nabla_i^2 + \sum_{i<j} v(r_{ij}). \tag{4.34}$$

For the helium two-body potential we have used that given by Aziz *et al.* [65]. Efficient PIMC simulations require many subtleties, but these are not discussed here further. A thorough review of path integral Monte Carlo simulations in liquid helium can be found in Ref. 66.

4.5.2 Kinetic energy of ^{3}He impurity in superfluid ^{4}He

We have only recently begun to do PIMC simulations on helium mixtures, and report here just the results for the kinetic energies of the two isotopes. In this subsection all energies are given in units of kelvin. By placing only a single ^{3}He impurity in ^{4}He, we avoid the fermion sign problem. We placed $N = 64$ atoms, of which one was ^{3}He, into a cubic volume with periodic boundary conditions to simulate a bulk system. Simulations with 32 atoms were also performed at some pressures and temperatures. It was noted that within statistical errors the results with the different number of atoms agree. We used a time step $\tau = 0.025$ K^{-1}, for which we and others have observed convergence, and computed the system at two temperatures $T = 0.25$ K and $T = 0.5$ K, and at six different densities. In our simulations we have exploited the Universal Path Integral code of D. M. Ceperley [67]. The obtained kinetic energies for the two isotopes and computed pressures are given in Table 4.1. It should be noted that in addition to statistical errors, some effects due to a finite size system also appear. An effort is made to compensate these, for example, in the case of pressure. Using PIMC, Boninsegni *et al.* found the kinetic energy of one ^{3}He in ^{4}He at temperature $T = 0.25$ K to be $K_3 = 17.4(3)$ K and $K_3 = 17.5(2)$ K for systems with $N = 54$ and $N = 108$ particles, respectively [41]. At $T = 0.5$ K they found similarly $K_3 = 18.1(3)$ K and $K_3 = 17.5(3)$ K. Our value for the kinetic energy is appreciably lower than theirs, by about one kelvin. They used a slightly higher density ($N/V = 0.0218$ Å^{-3}), but this explains only a fraction of the difference. Diffusion Monte Carlo simulations by Boronat *et al.* resulted in a zero temperature value of $K_3 = 18.4(5)$ K ($N/V = 0.0219$ Å^{-3}), which is clearly larger than

	$T = 0.25$ K			$T = 0.5$ K		
N/V (Å^{-3})	P (bar)	K_3 (K)	K_4 (K)	P (bar)	K_3 (K)	K_4 (K)
0.02174	0.28(8)	16.5(1)	13.73(2)	0.26(8)	16.6(1)	13.73(2)
0.0229	5.2(1)	18.0(1)	15.07(3)	5.1(1)	18.5(1)	15.12(2)
0.02382	10.3(2)	19.6(1)	16.22(3)	10.1(1)	19.9(1)	16.29(3)
0.02459	15.1(2)	20.7(1)	17.22(3)	15.4(2)	21.1(2)	17.24(3)
0.02526	20.0(2)	21.6(2)	18.12(3)	19.5(2)	22.2(2)	18.14(3)
0.02563	23.1(2)	22.1(1)	18.61(3)	23.0(2)	22.5(1)	18.65(4)

Table 4.1 Kinetic energies of ^{3}He K_3 and ^{4}He K_4 in units of K at temperatures $T = 0.25$ K and $T = 0.5$ K and various densities. The system includes $N = 64$ helium atoms, of which one is ^{3}He. Computed pressures are also given. Statistical errors (one standard deviation) given in parentheses apply to the last digits.

that of Boninsegni *et al.* [68]. Deep inelastic neutron scattering experiments place the value at around $K_3 = 12$ K [69–72]. This apparent discrepancy between various theoretical values [41, 68, 73, 74] and several experiments has not been resolved. For pure ^{4}He Boninsegni *et al.* found $K_4 = 14.3(1)$ K, compared to our value $K_4 = 13.73(2)$ K. The presence of ^{3}He tends to lower K_4.

The kinetic energies can be used to determine the chemical potential difference between the isotopes. At zero temperature the difference is [66]

$$\mu_3 - \mu_4 = \int_{m_3}^{m_4} \frac{K_m}{m} dm. \tag{4.35}$$

The kinetic energy of ^{3}He is extrapolated to zero temperature. We simply use the trapezoidal rule to evaluate this integral from our kinetic energy data at the two masses. The results are given in Table 4.2. By using experimental data for μ_4, we can compute μ_3 and further compare it with experiment. The experimental data are from [75]. Agreement between theory and experiment is quite good. This comparison is slightly hindered by the possible error in the calculated pressure due to finite size system.

We are particularly interested in the effective mass as a function of pressure, but for some, yet unsolved, reason, our obtained effective masses for the ^{3}He impurity were unexpectedly large by a factor of approximately 1.7 compared to experiments and earlier calculations. This may be due to some problem with the effective mass estimator, since all the other quantities seemed sensible. RPIMC simulations, with larger amount of ^{3}He atoms in the system, might provide information about the effective ^{3}He–^{3}He interactions and could perhaps be compared to our phenomenological results.

N/V (Å^{-3})	P (bar)	$\mu_3 - \mu_4$ (K)	μ_4 expt (K)	μ_3 (K)	μ_3 expt (K)
0.02174	0.28(8)	4.4	-7.17	-2.8	-2.66
0.0229	5.2(1)	4.7	-5.49	-0.8	-0.65
0.02382	10.3(2)	5.1	-3.92	1.2	1.28
0.02459	15.1(2)	5.5	-2.45	3.0	3.00
0.02526	20.0(2)	5.7	-1.00	4.7	4.69
0.02563	23.1(2)	5.9	0.02	5.9	5.73

Table 4.2 Chemical potential difference of the two isotopes, $\mu_3 - \mu_4$, calculated from Eq. (4.35). The chemical potential of ^{3}He is obtained by utilizing experimental data for μ_4. Experimental values are denoted by "expt". The simulated pressures are also given. All chemical potentials are in units of kelvin. The statistical error in the computed chemical potentials are of the order ± 0.2 K. Statistical errors for the pressures given in parentheses apply to the last digits. Experimental data are from Ref. 75.

Chapter 5

Quartz Tuning Fork

Quartz tuning forks are commercially mass produced components, which are meant for frequency standards in various devices, such as watches. They employ the piezoelectric properties of quartz (crystalline SiO_2); application of electric field on the crystal causes mechanical stress. When the crystal is properly cut and shaped, it can resonate with certain resonant frequencies. These oscillators have the shape of a traditional tuning fork, hence the name. Large number of possible resonant modes exist, but the most commonly used is the one, where the two tines oscillate in antiphase toward each other with no nodes along the tines. The frequency of this mode varies between different quartz tuning fork models, but the most common intended frequency is exactly 2^{15} Hz ($= 32\,768$ Hz) at room temperature. To excite the proper resonant mode, metal electrodes have been placed on the surface of the tines.

Mechanical resonators of different kinds have long been used to probe the properties of superfluid helium. When the oscillator is immersed in a fluid medium, the oscillator response changes due to additional inertia and dissipation compared to vacuum environment. Traditionally conducting wires forming a half circle and placed in a magnetic field have been used for this purpose [76]. Vibrating grids [77] and levitating spheres [78] have also been studied. In recent years quartz tuning forks have gained much popularity over vibrating wires due to their many advantages. They are easy to operate, since they do not require a magnetic field, and are in fact very insensitive to external fields. As mass-produced items they are readily available and they have a superior quality factor and stability. The quality factor of a resonator is defined as the ratio of the resonant frequency to the width of the resonance curve at half maximum, $Q = f_0/\Delta f$. Smaller density of quartz ($\rho_q \approx 2659$ kg/m^3) compared to metallic vibrating wires offer larger changes in frequency due to the surrounding medium, thus improving sensitivity. Quartz tuning forks with smaller physical size (smaller oscillator mass)

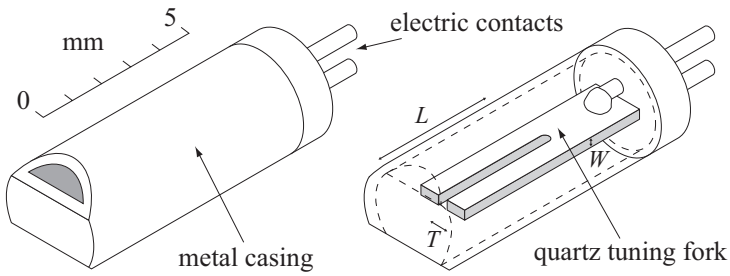

Fig. 5.1 Quartz tuning fork and its container. The dimensions correspond to a Fox Electronics NC38 quartz tuning fork, used in some of our experiments. Dimensions of the oscillator itself are $T = 0.60$ mm, $W = 0.34$ mm, and $L = 3.76$ mm. The space between the tines is 0.30 mm. Two holes have been created at the end of the metal casing to allow contact between the resonator and surrounding fluid. In NC38 quartz tuning fork, excitation and detection wires are connected on different sides of the base.

can be used in a low viscosity fluid and larger models are more suited at larger viscosities. The main disadvantage of a tuning fork resonator is its rather complicated geometry, which hinders analytical approaches to the evaluation of its resonant properties. Since the introduction of quartz tuning forks in low temperature helium research by Clubb *et al.* [10], they have been used to measure, for example, temperature, pressure, viscosity, and turbulence in superfluid helium [11, 79, 80].

In production, quartz tuning forks are encapsulated in hermetically sealed metallic containers, often with a cylindrical shape. A schematic drawing of a quartz tuning fork with the dimensions appropriate to a Fox Electronics model NC38 is shown in Fig. 5.1. To make contact between the oscillator and sample, the hermetic container must be breached. It can either be removed completely, or holes can be created on it. In Fig. 5.1, holes have been filed on both sides of the top of the container. This is the main configuration we have used in our experiments. As will be noted in the following sections, the container has a significant effect on the resonant characteristics due to first and second sound resonances in the cavity. The excitation and detection wires have been cast inside a ceramic plug. In NC38 quartz tuning fork, the wires are connected on different sides of the oscillator base, but in some models they are on the same side next to each other.

In our measurement setup we apply a sinusoidal excitation voltage from a function generator to the quartz tuning fork and a reference signal to a lock-in amplifier. The detection signal is filtered and amplified before arriving at the lock-in.

Another widely used option is to connect a current-to-voltage converter before the lock-in amplifier. We observed that by connecting a small capacitor between the excitation wire and ground, the residual width of the resonance could be reduced. An optimum amount of capacitance exists, which maximizes the Q-value. It should be noted, however, that this effect is likely due to the properties of the measurement setup, not the oscillator. Also removing the dielectric insulator from a coaxial cable and replacing it with a fiberglass sleeving reduced the width. These procedures can increase the quality factor in vacuum at low temperature to such a large value that it is difficult to even measure. Without these additional width-reduction measures, it is still quite large, typically $Q \sim 10^6$.

The appropriate description of the effect of surrounding fluid on the oscillator depends on the mean free path of the excitations. At relatively high temperatures, when the mean free path is small compared to the oscillator dimensions, a hydrodynamical model can be applied. In the hydrodynamical regime, the resonant frequency f_0 of a mechanical oscillator immersed in a viscous fluid with viscosity η is given by [11]

$$f_0 = f_{0\mathrm{vac}} \left[1 + \frac{\rho_\mathrm{F}}{\rho_\mathrm{S}} \left(B + \beta \frac{S}{V} \sqrt{\frac{\eta}{\pi \rho_\mathrm{F} f_0}} \right) \right]^{-1/2}, \tag{5.1}$$

where $f_{0\mathrm{vac}}$ is the resonant frequency in vacuum, B and β are geometry-dependent dimensionless factors of order one, and ρ_F and ρ_S are the densities of the fluid and the oscillator (solid), respectively. The other geometry factors are defined as $S = 2(T+W)L$ and $V = TWL$, representing the area and volume of one tine. The dimensions T, W, and L are defined in Fig. 5.1. Width of the resonance is given by

$$\Delta f = \Delta f_\mathrm{invisc} + \frac{1}{2} CS \sqrt{\frac{\rho_\mathrm{F} \eta f_0}{\pi}} \frac{(f_0/f_{0\mathrm{vac}})^2}{m^*}, \tag{5.2}$$

where Δf_invisc includes all contributions to the width besides viscosity, such as acoustic emission and internal damping of the oscillator.

At low temperatures this hydrodynamic description is no longer valid as the mean free path increases. The quasiparticle gas becomes a collection of ballistic entities and viscosity is not a suitable concept anymore. At sufficiently low temperatures and small oscillation velocities in superfluid ^{3}He, the width of the resonance is $\propto e^{-\Delta/k_\mathrm{B}T}$, where Δ is the superfluid energy gap. The zero pressure value of the gap is $\Delta = 1.77\ k_\mathrm{B}T_\mathrm{c}$ [81], has a linear density dependence [35], and is $\Delta = 1.99\ k_\mathrm{B}T_\mathrm{c}$ at the melting pressure [82]. Simulations of even simple geometries, such as vibrating wires, in the fully ballistic regime are cumbersome [83, 84].

At small oscillation amplitudes, the motion of a quartz tuning fork can be modeled as a harmonic oscillator with an effective mass. We can use the equation of motion of a driven damped harmonic oscillator

$$F_{\mathrm{e}} = m\frac{d^2x}{dt^2} + m\gamma\frac{dx}{dt} + k_{\mathrm{s}}x, \tag{5.3}$$

where F_{e} is the excitation force, m is the mass of the oscillator (one tine), x is the displacement, k_{s} is the spring constant, and γ represents damping. If the oscillator is in vacuum, γ stands for internal damping of the oscillator. The resonant frequency is given by

$$f_0 = \frac{1}{2\pi}\sqrt{\frac{k_{\mathrm{s}}}{m}}. \tag{5.4}$$

Since the tuning fork is effectively composed of two cantilever beams, we cannot use Eqs. (5.3) and (5.4) directly with the mass of a tine. Instead we must use an effective mass [85]

$$m^* = 0.2427m, \tag{5.5}$$

which applies to a uniform rectangular beam fixed at its base. The spring constant is

$$k_{\mathrm{s}} = \frac{E}{4}W\left(\frac{T}{L}\right)^3, \tag{5.6}$$

where E is the elastic modulus, which for quartz at room temperature is $E = 7.87 \cdot 10^{10}$ Pa. Using the dimensions of NC38, the above equation gives a resonant frequency $f_0 = 37505$ Hz, which is 14% larger than the measured value at room temperature. Some of the discrepancy is likely due to the the added mass of the electrodes, difference in the actual elastic modulus and deviations of the real geometry compared to the model [11], but a significant effect is also due to the assumption of a fixed cantilever beam, as will be noted below.

As was mentioned, a quartz tuning fork can oscillate in a large number of resonant modes with increasing frequencies. We can determine the eigenmodes and eigenfrequencies by using a linear elastic material model and the finite element method (FEM). For this purpose we have used Comsol Multiphysics software. Twelve lowest-frequency tuning fork modes for an oscillator, which is fixed only from the bottom of its base, are given in Fig. 5.2. The primary mode is the one with frequency 30 790 Hz. This is 6% smaller than the measured value and 18% smaller than the one given by the effective cantilever model. The large discrepancy between the two models is explained by the fact that the cantilever model assumes the tines to be fixed at one end. By fixing the tines similarly in the simulation, the resonant frequency changes to 36 870 Hz, which is only 1.5% smaller

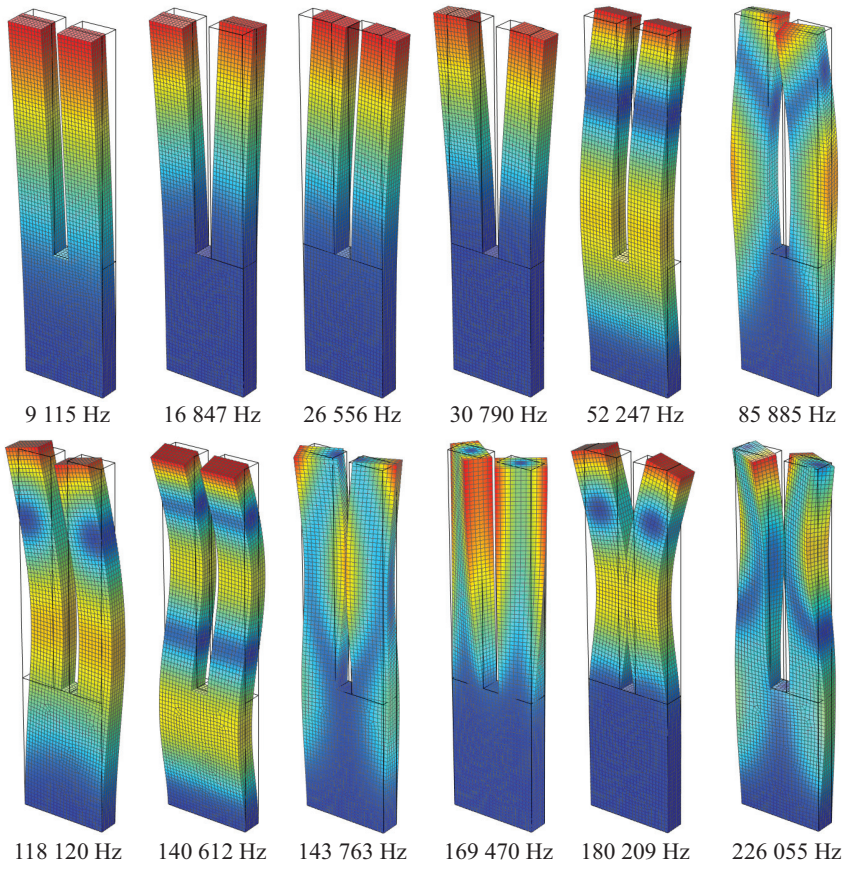

Fig. 5.2 The lowest twelve eigenmodes of a quartz tuning fork with dimensions consistent with a Fox Electronics NC38. The corresponding eigenfrequencies are given below each mode. The tuning fork has been fixed at the bottom of the base. Color is a measure of displacement from the rest position, blue indicating zero displacement. The amplitudes have been greatly exaggerated to bring out the shapes clearly. The rest position is also seen as a black frame. Due to the electrode configuration on the tines, only the modes with eigenfrequencies 30 790 Hz and 180 209 Hz can be excited.

than that given by the effective model. If we take into account the actual half circular shape between the tines, the obtained frequency is 31 770 Hz, which brings the difference between measured and calculated values to 3%. This can with confidence be attributed to the effects mentioned earlier.

The electrodes on the surface of the quartz tuning fork tines are manufactured so that the applied voltage can excite the 31 kHz mode, that is, symmetrically in antiphase. Therefore, most of the other modes cannot be excited with such electrode configuration. The next available mode is at 180 209 Hz. We have performed measurements with this mode as well. The quality factor is not quite as good as it is for the first mode, and at higher frequency, heat release to the sample is larger.

5.1 Effect of helium exposure

In this section we briefly note an effect, which was observed when a quartz tuning fork was exposed to gaseous helium at room temperature. When the oscillator was subjected to helium gas, the resonant frequency increased slowly with a time constant of several hours. At a pressure of approximately one atmosphere, it saturated to about 35 mHz higher frequency. At higher pressures, the effect was significantly stronger. A four-day exposure to 10 bar room temperature helium raised the frequency by approximately 2 Hz. When the tuning fork cavity was evacuated from helium, reverse effect was observed with a different time constant. For the low pressure exposure, the time constant was shorter, but it took more than a month for the oscillator to recover from the 10 bar helium environment. At liquid nitrogen temperature (77 K), the effect was significantly smaller and slower. This increase in frequency was observed every time the tuning fork was exposed to room temperature helium, but could not be exactly reproduced. The width remained almost constant with perhaps a tiny decrease when in helium. Neon had no such effect on the tuning fork frequency.

One possibility is diffusion of helium into quartz crystal. The diffusion mechanism of helium in quartz is not very well understood and measured diffusion constants differ by orders of magnitude [86]. According to molecular dynamics simulations, structural defects can significantly affect the mobility of helium atoms in quartz [87]. From Eqs. (5.4) and (5.6) we see that the resonant frequency of a quartz tuning fork in vacuum is

$$f_{0\mathrm{vac}} = \frac{aT}{L^2}\sqrt{\frac{E}{\rho_\mathrm{q}}}, \tag{5.7}$$

where a is a constant. From the above equation, one can observe that the vacuum resonant frequency can increase if E increases, ρ_q decreases, or all oscillator dimensions grow by an equal amount. The last case corresponds to the situation, where the increase in volume occurs only on the surfaces of the tuning fork. One might think at first that diffusing helium would increase the density and thus decrease the frequency. But perhaps a stronger effect is an increase in the elastic modulus. It seems that the rate of diffusion is too slow to explain the effect, which thus remains unexplained. We did not investigate this in greater detail, but feel that it is worth noting here.

Chapter 6

Propagation of Sound in Helium

6.1 First sound

Compressibility of a medium leads to propagation of density (pressure) waves, called first sound. This is the ordinary sound encountered in many different physical systems and in everyday life. Compressible fluid also changes the response of an oscillating object compared to incompressible medium. For simplicity, we neglect viscosity and set $\eta = 0$ in Eq. (5.1) to obtain

$$f_0 = f_{0\mathrm{vac}} \left(1 + B\frac{\rho_\mathrm{F}}{\rho_\mathrm{S}} \right)^{-1/2}. \tag{6.1}$$

When the wavelength of sound in the fluid is much larger than the relevant dimensions of the oscillator, the fluid is often assumed to be incompressible. Under this approximation, B is a constant, which depends only on the oscillator geometry. In precise measurements this assumption cannot be made even if the wavelength is an order of magnitude larger than the dimensions. The situation becomes even more tricky if acoustic resonances in the cavity around the oscillator or within the oscillator geometry are present. When compressibility is taken into account, the geometrical factor B becomes dependent on the wavelength (wave vector) of sound in the medium. Knowledge of this factor is essential in analyzing the resonator response to the surrounding fluid. Unfortunately B can be determined analytically only for some simple geometries. An example is a single infinitely long circular beam oscillating in infinite medium. The geometry of a quartz tuning fork is much too complicated for fully analytical approaches. We are thus restricted to numerical methods when finding the geometrical factor in various situations.

To understand the behavior of quartz tuning forks, or other oscillators, immersed in compressible fluids, we have performed numerical simulations using the finite element method. This numerical method is well suited for simulations with complicated geometry. The numerical computations have been performed with Comsol Multiphysics using a desktop computer. The surrounding fluid was modeled as an acoustic medium, which obeys the Helmholtz equation

$$\nabla^2 P - k^2 P = 0. \tag{6.2}$$

Here P is the acoustic pressure (small deviation from an equilibrium value) and $k = \omega/c = 2\pi/\lambda$ is the acoustic wave vector. The most common resonant frequency of the lowest usable mode of a quartz tuning fork (*cf.* Fig. 5.2) is about 32 kHz, but a wide range of different-sized oscillators with different frequencies exist. Speed of first sound in helium liquids vary between 100 m/s and 400 m/s. Thus, a 32 kHz tuning fork can cover a wave vector range between $k = 500$ m^{-1} and 2000 m^{-1}. Higher-frequency oscillators allow one to perform experiments at wave vector values in the several thousands. Thus, depending on the quartz tuning fork model, a large range of wavelengths is accessible.

We have simulated various oscillator geometries immersed in infinite medium and inside a fluid-filled container. Infinite medium is modeled by an artificial boundary, where the boundary condition results in minimal reflection of acoustic waves. We have considered both infinitely long oscillating objects, which reduces the problem to 2D, and the full 3D quartz tuning fork geometry. The 2D simulations are computationally considerably less demanding than those in 3D. We verified our computational method by solving the case of an infinite circular cylinder in infinite compressible medium analytically and compared our simulated results to it. Agreement was found to be nearly perfect. These simulations can help in analyzing the data from quartz tuning forks and to choose a resonator with appropriate size, relative dimensions, and resonant frequency. In addition to obtaining the geometrical factor, we can also study acoustic emission due to the oscillating object in our simulations. The acoustic field of a quartz tuning fork is shown in Fig. 6.1. Emitted acoustic power is directly related to the width of the oscillator resonance compared to the width in vacuum. Strong frequency dependence is a characteristic property of acoustic emission, typically following a power law at low wave vectors, $\propto k^p$ with $p \sim 5$. We investigated the effect of different resonator geometries on the acoustic emission. These results are reported in publications **V** and **VI**. For a Fox Electronics NC38 quartz tuning fork, we found an exponent $p = 4.87$. This is comparable to a value obtained experimentally by Schmoranzer *et al.* for several different quartz tuning fork models, $p \approx 5.6$ [88]. The scatter in their experimental data does permit an exponent somewhat below 5. Modeling the tuning fork acoustic emission as

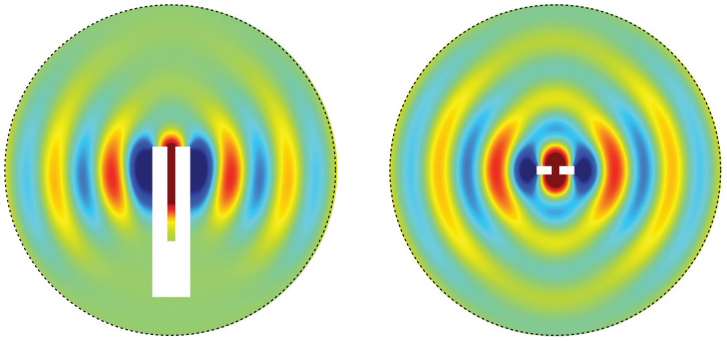

Fig. 6.1 Acoustic field in 3D quartz tuning fork simulations shown from two directions. The colors represent the value of the pressure amplitude (red for positive and blue for negative), which varies sinusoidally in time around an equilibrium value (green). The boundary condition on the dashed boundaries mimics that of an infinite medium. The wave vector corresponding to the oscillator's vacuum resonant frequency in this case is $k = 2550\ \mathrm{m}^{-1}$.

3D and 2D quadrupole source and as emission from two infinite cylinders, these authors found $p = 6$ (3D), $p = 5$ (2D), and $p = 5$ (two cylinders).

A general property of B for all oscillators in infinite medium is, that it is rather constant at low wave vectors (incompressible limit), grows as a function of k, assumes a maximum at some wavelength, and finally begins to decrease. If there are no acoustic resonant modes within the oscillator structures, the value of B goes steadily to zero in the limit $k \to \infty$ (infinite compressibility). Acoustic resonances within the bound fluid cavity around the resonator complicate the oscillator response drastically. The geometrical factor can even become multivalued and negative due to a resonance. A negative B means that the resonant frequency of the oscillator is larger than in vacuum. This was suggested by our simulations and has also been observed experimentally [89]. A complication for comparison between simulations and experiments is the usually unknown asymmetrical position of the tuning fork in the container. By removing the casing of one NC38 quartz tuning fork, it was observed that it had a rather large tilt of approximately 5 degrees in one direction. Possible tilt in the other direction could not be resolved. A tilted tuning fork breaks symmetries in the cavity and allows more resonant modes to be excited by the oscillator. Also the closer proximity of the container walls to the tine tips tends to increase the geometrical factor. Comparison between a simulation and experiment is illustrated in Fig. 6.2. The figure shows the computed results for both symmetrical and realistically tilted

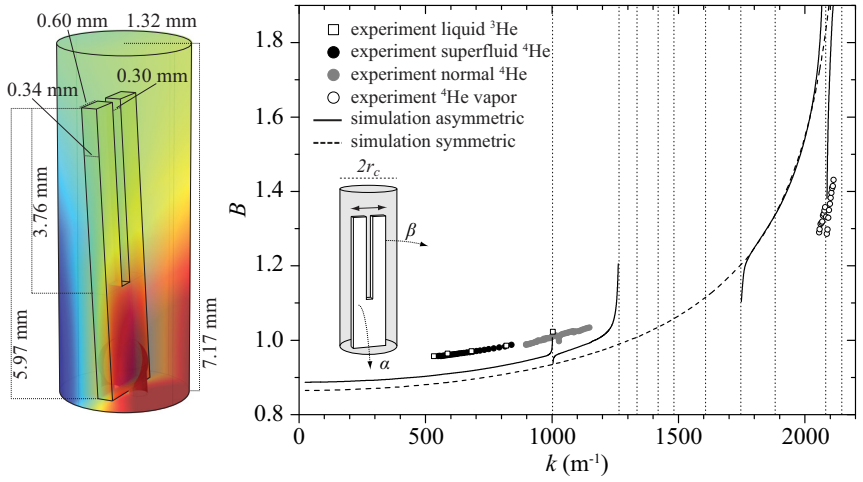

Fig. 6.2 Simulated and measured geometrical factor B of a Fox Electronics NC38 quartz tuning fork. The solid curve is the computed response of a tilted oscillator, with $\alpha = 4°$ and $\beta = 2°$. The simulation has not been carried out between $k = 1250\ \mathrm{m}^{-1}$ and $k = 1750\ \mathrm{m}^{-1}$ and beyond $k = 2100\ \mathrm{m}^{-1}$ because this becomes tedious around acoustic resonances. The dashed curve is for symmetrically positioned tuning fork, which behaves regularly enough to be simulated throughout that range. Experimental data are from [21, 90]. The left-hand figure illustrates one resonant mode, which is not excited unless the tuning fork is tilted in both directions.

cases. We see that tilting the oscillator in the simulations decreases the degree of discrepancy to the experiment. It seems likely that some of the features in the experimental data are due to first sound resonances in the tuning fork capsule. The figure also depicts as an example one resonant mode in the container, which is not excited unless the tuning fork is tilted in both directions.

6.2 Second sound

In addition to first sound, liquid helium in its superfluid state can support another type of wave motion called second sound. Motivated by Kapitza's, Allen and Misener's, and others' experimental results [91–94], Tisza [95–97] and later Landau [98, 99] postulated that superfluid helium-4 can be considered to be composed of two intermixed fluids, the superfluid component and the normal fluid component. These two fluids can move freely with respect to each other without any viscous interaction. This model should not be taken too literally, but it has

been found to be very powerful. In helium mixtures, the normal fluid component consists of a "gas" of the elementary excitations, phonons, rotons, and ^{3}He quasiparticles in a background superfluid ^{4}He. Second sound is a density wave of this excitation gas. It propagates so that the total mass density remains constant. At low temperatures ($T \lesssim 0.7$ K) ^{4}He is practically 100% superfluid and second sound is a ^{3}He concentration wave. Because the superfluid component does not carry any entropy, second sound can also be considered as an entropy wave or temperature wave.

When a quartz tuning fork left in its capsule was used to measure helium mixtures, strong anomalies in the resonant behavior were unexpectedly observed. These anomalies were interpreted to result from second sound resonances in the cavity. Some experimental data are shown in Fig. 6.3. The upper figures show the resonant frequency and width of a quartz tuning fork in approximately 8% mixture over a temperature sweep between 100 mK and 1.9 K. Several overlapping resonant peaks are observed. The lower images illustrate how the resonances change as ^{3}He is added. It seems as if the modes present in pure ^{4}He disappear and new, stronger ones, appear. The "pure ^{4}He modes" shift slightly to lower temperatures as x increases and the mixture modes shift to higher temperatures. The modes in pure ^{4}He are extremely narrow, and one must be very close to the correct temperature in order to observe them. All these apparent second sound resonances are very well reproducible and have a temperature resolution of order 1 μK. Therefore, these very distinct features offer a possible means of constructing an accurate thermometer, for example, by sealing a certain composition of helium isotopes inside a container with quartz tuning forks.

A distinct feature in the data of the upper panels of Fig. 6.3 is a symmetry point at about $T = 1.2$ K. This is obviously the result of a maximum in the speed of second sound as a function of temperature. Thus, the resonance data can be used to determine the sound speed on one side of this maximum if it is known on the other side. Results of such analysis are shown in Fig. 6.4. It includes data for pure ^{4}He and various concentrations of ^{3}He. Pure ^{4}He has a local maximum at approximately 1.7 K. At zero temperature the velocity tends to a value $u_2 = u_1/\sqrt{3}$ [105], where u_1 is the speed of first sound, but second sound becomes insignificant in pure ^{4}He below about 0.7 K as the amount of normal fluid diminishes.

To get a basic understanding of sound modes in a quartz tuning fork container we can solve the eigenmodes of the Helmholtz equation, Eq. (6.2), in the fluid volume to find the shapes of the resonant modes in the cavity. This was done in publication **IX**. Since the wavelength of second sound in the region of interest is comparable to the relevant dimensions of the quartz tuning fork, many reso-

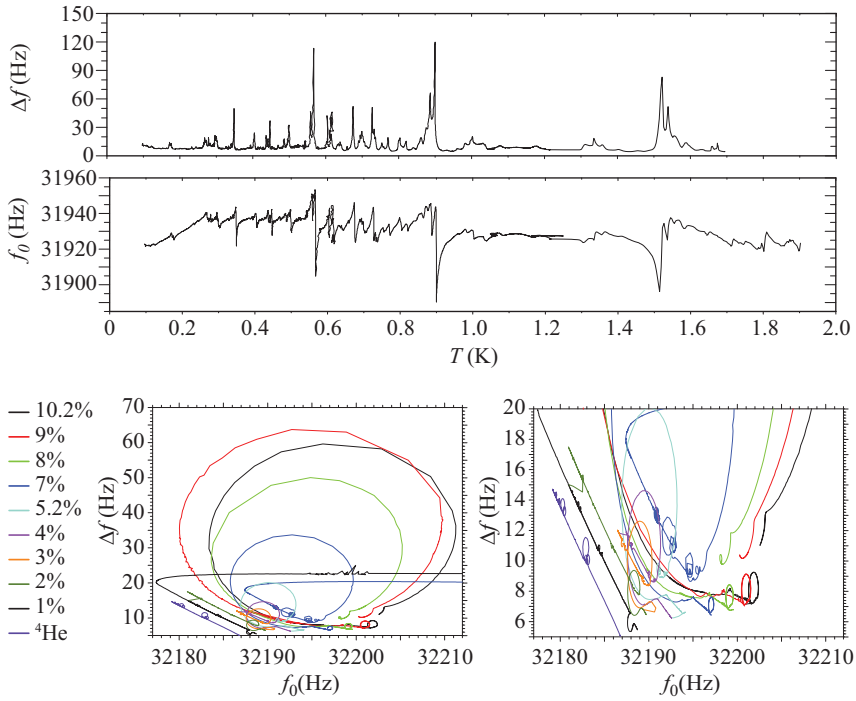

Fig. 6.3 Measured second sound resonances inside a cylindrical quartz tuning fork capsule. The upper figures display the resonant frequency and width of a Fox Electronics NC38 in approximately 8% mixture over a large range of temperatures. The bottom figures depict the width of the resonance as a function of frequency of an ECS-1x5x quartz tuning fork at many compositions, ranging from pure ^{4}He to 10% mixture, as temperature is varied between 1.4 K and 2.1 K. Acoustic resonances produce loops in such a plot. The bottom right figure shows a close-up of the smaller loops.

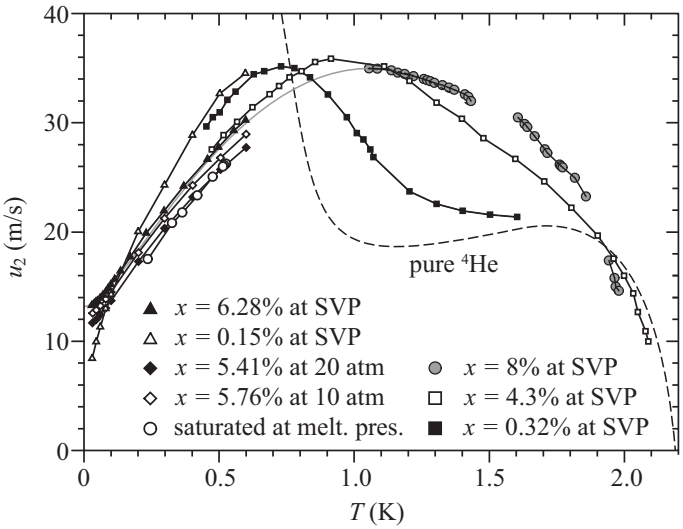

Fig. 6.4 Experimental results for the speed of second sound in helium liquids. The dashed line is for pure ^{4}He at SVP [100–102], while the various points are for different concentrations of ^{3}He in ^{4}He; 0.32% and 4.3% [103] and 0.15%, 6.28%, 5.76%, and 5.41% [104]. The grey dots are our results for approximately 8% mixture above 1.1 K based on the assumed dependence below 1.05 K (grey line) [**IV**].

nant modes exist in close proximity. The eigenmodes have been normalized by the RMS value of the "pressure field". We can estimate the relative coupling strength of different modes by integrating the field on the tuning fork tines and weighing it properly. Some of the eigenmodes are shown in Fig. 6.5, where the corresponding wavelength is given. As can be seen, the modes at these wavelengths are quite complicated. This approach does not consider at all how these modes are excited by the oscillator. A more complete model can be constructed with the two-fluid model to be described in the next section.

6.2.1 Hydrodynamical equations

In this and the following subsection we report some preliminary results from our investigations of second sound excitation by quartz tuning forks. In the two fluid model it is assumed that superfluid helium-4 behaves as if it were a mixture of two fluids, the normal fluid and the superfluid, freely intermingling with each other without any viscous interaction [106]. It is assumed that at each point

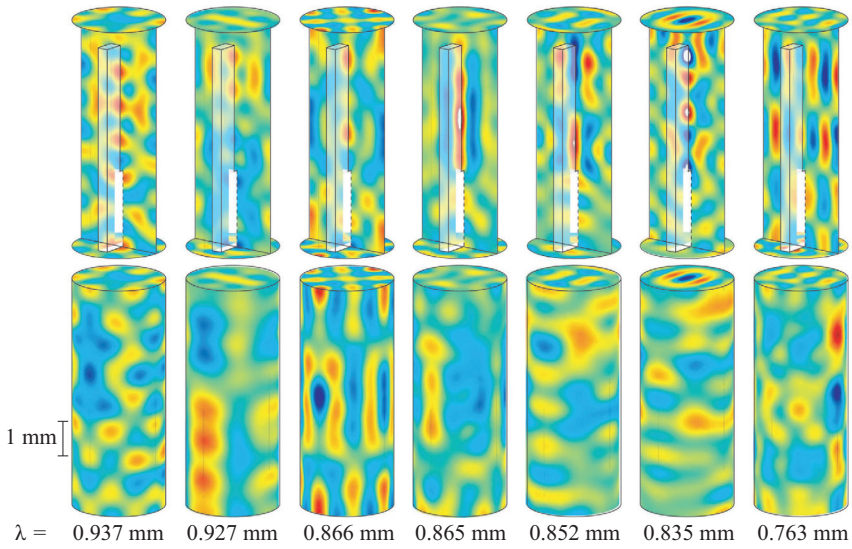

Fig. 6.5 Some of the most strongly coupling acoustic modes in a quartz tuning fork container with the oscillator placed symmetrically in the cavity. Blue and red colors indicate antinodes of the sound wave. The upper row shows sliced images, while the lower shows the container surface. The appropriate wavelengths are given below the images.

in the fluid there are two independent velocity fields. In helium mixtures it is further assumed that the impurity atoms (^{3}He) move along with the normal component of ^{4}He. In the case of dilute mixtures, this has been proven rigorously to be correct [107]. The above assumption is valid only when ^{3}He remains normal. Thus, if the superfluid state of helium mixtures is discovered, it is possible to realize three different motions in the fluid; one normal velocity and two superfluid velocities.

According to the two fluid model, the total density of the liquid is a sum of two components

$$\rho = \rho_{\mathrm{s}} + \rho_{\mathrm{n}}, \tag{6.3}$$

where ρ_{s} is the density of the superfluid component and ρ_{n} the density of the normal component. It is assumed that the motions of these two components are decoupled, that is, there are two velocity fields within the fluid; the superfluid and normal fluid velocities $\vec{v}_{\mathrm{s}}$ and $\vec{v}_{\mathrm{n}}$. The total mass flux is defined as

$$\vec{j} = \rho_{\mathrm{s}}\vec{v}_{\mathrm{s}} + \rho_{\mathrm{n}}\vec{v}_{\mathrm{n}}. \tag{6.4}$$

We consider a small disturbance from a steady state in which $\vec{v_n} = \vec{v_s} = 0$ and neglect any second order terms. The linearized two-fluid equations without dissipation are, as given by Khalatnikov [107],

$$\frac{\partial \rho}{\partial t} + \nabla \cdot \vec{j} = 0, \tag{6.5}$$

$$\frac{\partial \vec{j}}{\partial t} + \nabla P = 0, \tag{6.6}$$

$$\frac{\partial (\rho \sigma)}{\partial t} + \rho \sigma \nabla \cdot \vec{v_n} = 0, \tag{6.7}$$

$$\frac{\partial (\rho c)}{\partial t} + \rho c \nabla \cdot \vec{v_n} = 0, \tag{6.8}$$

$$\frac{\partial \vec{v_s}}{\partial t} + \nabla \left(\mu - \frac{Z}{\rho} c \right) = 0. \tag{6.9}$$

These equations are written in terms of the mass concentration

$$c = \frac{m_3 N_3}{m_3 N_3 + m_4 N_4}, \tag{6.10}$$

which is connected to the molar concentration x through

$$c = \frac{x m_3}{m_4 - x(m_4 - m_3)}. \tag{6.11}$$

The first of the five linearized two-fluid equations represents mass conservation. The second equation is due to conservation of momentum. Eq. (6.7) is the conservation of entropy and Eq. (6.8) is the continuity equation for the impurity (^{3}He). The last equation states the fact that chemical potential is the driving force for the superfluid component. Here $\mu = c\mu_3 + (1-c)\mu_4$ is the specific chemical potential (chemical potential per mass), and μ_3 and μ_4 are the specific chemical potentials of the components. Further, $Z = \rho(\mu_3 - \mu_4)$ and the last equation can thus also be written as

$$\frac{\partial \vec{v_s}}{\partial t} + \nabla \mu_4 = 0, \tag{6.12}$$

which recapitulates that the superfluid component is driven by the chemical potential gradient of ^{4}He. It can be regarded as the "superfluid acceleration potential". The equations above use the specific entropy $\sigma \equiv s/\rho$, where s is the entropy density.

By using $d\mu = -\sigma dT + dP/\rho \Rightarrow \nabla\mu = -\sigma\nabla T + \nabla P/\rho$ and eliminating the velocities from the hydrodynamical equations, we obtain three relations

$$\frac{\partial^2\rho}{\partial t^2} = \nabla^2 P, \tag{6.13}$$

$$\frac{\rho_{\rm n}}{\rho_{\rm s}\sigma}\frac{\partial^2\sigma}{\partial t^2} = \sigma\nabla^2 T + c\nabla^2\left(\frac{Z}{\rho}\right), \tag{6.14}$$

$$\frac{1}{c}\frac{\partial c}{\partial t} = \frac{1}{\sigma}\frac{\partial\sigma}{\partial t}. \tag{6.15}$$

We choose T, P, and c as our independent variables and consider small perturbations around an equilibrium value. We thus write $T = T_0 + \widetilde{T}(\vec{r},t)$, and similarly for all the other variables. The density in terms of the three independent variables is

$$\widetilde{\rho} = \left(\frac{\partial\rho}{\partial T}\right)_{P,c}\widetilde{T} + \left(\frac{\partial\rho}{\partial P}\right)_{T,c}\widetilde{P} + \left(\frac{\partial\rho}{\partial c}\right)_{T,P}\widetilde{c} \tag{6.16}$$

and similarly for $\widetilde{\sigma}$ and $\widetilde{Z/\rho}$. We further assume sinusoidal time-dependence $\propto e^{-i\omega t}$ for all the variables. The resulting equations are

$$\frac{1}{\omega^2}\nabla^2\widetilde{P} + \left(\frac{\partial\rho}{\partial T}\right)\widetilde{T} + \left(\frac{\partial\rho}{\partial P}\right)\widetilde{P} + \left(\frac{\partial\rho}{\partial c}\right)\widetilde{c} = 0, \tag{6.17}$$

$$\begin{aligned}\bar{\sigma}\nabla^2\widetilde{T} - \frac{c_0}{\rho^2}\left(\frac{\partial\rho}{\partial c}\right)\nabla^2\widetilde{P} + c_0\left(\frac{\partial(Z/\rho)}{\partial c}\right)\nabla^2\widetilde{c} \\ + \frac{\rho_{\rm n}\omega^2}{\rho_{\rm s}\sigma}\left[\left(\frac{\partial\sigma}{\partial T}\right)\widetilde{T} + \frac{1}{\rho^2}\left(\frac{\partial\rho}{\partial T}\right)\widetilde{P} + \left(\frac{\sigma_0-\bar{\sigma}}{c_0}\right)\widetilde{c}\right] = 0,\end{aligned} \tag{6.18}$$

$$c_0\left(\frac{\partial\sigma}{\partial T}\right)\widetilde{T} + \frac{c_0}{\rho^2}\left(\frac{\partial P}{\partial T}\right)\widetilde{P} - \bar{\sigma}\widetilde{c} = 0. \tag{6.19}$$

Here we have used the Maxwell relations

$$\begin{cases}\partial(Z/\rho)/\partial P = -1/\rho^2\partial\rho/\partial c \\ \partial(Z/\rho)/\partial T = -\partial\sigma/\partial c \\ \partial\sigma/\partial P = 1/\rho^2\partial\rho/\partial T\end{cases} \tag{6.20}$$

obtained from $d\mu = 1/\rho dP - \sigma dT + (Z/\rho)dc$. We have also defined $\bar{\sigma} \equiv \sigma - c_0(\partial\sigma/\partial c)$. When we further eliminate $\widetilde{c}$ from above, we have equations of the form

$$\beta_{11}\nabla^2\widetilde{P} + \alpha_{12}\widetilde{T} + \beta_{12}\widetilde{P} = 0, \tag{6.21}$$

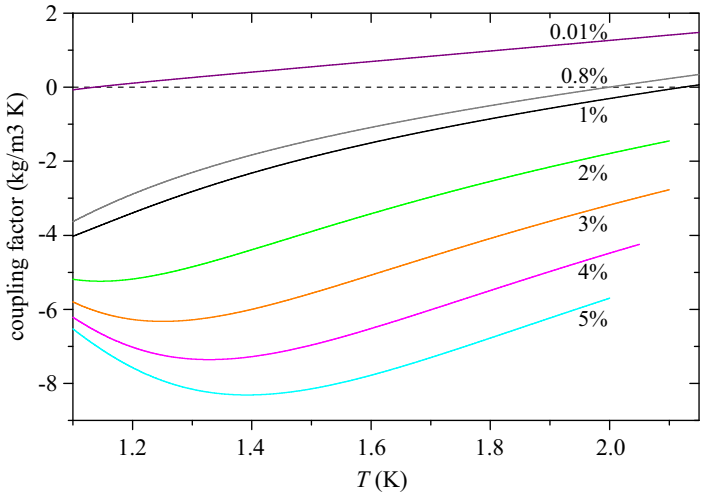

Fig. 6.6 Coupling factor α_{12} of Eq. (6.23) between second sound and first sound for various concentrations and temperatures between 1.1 K and 2.1 K.

$$\alpha_{21}\nabla^2\widetilde{T}+\beta_{21}\nabla^2\widetilde{P}+\alpha_{22}\widetilde{T}+\beta_{22}\widetilde{P}=0. \tag{6.22}$$

We see that the coupling term between second sound and first sound is α_{12}, which is given by

$$\alpha_{12}=\left(\frac{\partial\rho}{\partial T}\right)+\frac{c_0}{\bar{\sigma}}\left(\frac{\partial\rho}{\partial c}\right)\left(\frac{\partial\sigma}{\partial T}\right). \tag{6.23}$$

The absolute value of this factor represents how strongly second sound couples to first sound. Its sign only affects the phase between them. Coupling in pure ^{4}He is solely related to $\partial\rho/\partial T$, which is quite small, except around T_λ. In mixtures at large concentrations the coupling is governed by the second term. Since $\partial\rho/\partial T>0$, $c/\bar{\sigma}>0$, $\partial\rho/\partial c<0$, and $\partial\sigma/\partial T>0$, it is possible that for some concentration, cancelation occurs and the two sound modes decouple from each other. Brusov *et al.* investigated sound conversion in helium mixtures [108], but they apparently made a sign error in writing α_{12}, which prevented them from noticing this. The coupling factor, calculated by using the ideal solution approximation and experimental data to be discussed below, is given in Fig. 6.6. For pure ^{4}He (in the simulation 0.01%), coupling is rather small, except near T_λ. The coupling factor for ^{4}He should in fact go to zero faster than what is indicated in Fig. 6.6, because of our inaccurate fit to experimental data. This feature does not

have much significance to our conclusions of this section. We intend to refine our preliminary simulations and fix this mistake along with other improvements. As concentration increases, the coupling factor becomes more negative. It seems to have a minimum as a function of temperature at large enough concentrations. Whether this is a real effect or simply due to approximations in our model, is under investigation. Nevertheless it seems that for some temperatures and concentrations the terms in the coupling factor cancel and the sound modes decouple from one another. The factor for $x = 0.8\%$ is almost zero in the important temperature region for strong second sound resonances (~ 2 K), thus second sound resonances are expected to be suppressed at that concentration.

For the preliminary calculations presented in this section, we assume that the helium isotopes form an ideal solution, *i.e.* a solution, where the components do not interact with one another. The specific entropy can then be written as

$$\sigma = (1-c)\sigma_{40} + c\sigma_{30} - \frac{k_B}{m_4}(1-c)\ln(1-x) - \frac{k_B}{m_3}c\ln x \tag{6.24}$$

and consequently

$$\bar{\sigma} = \sigma_{40} - \frac{k_B}{m_4}\ln(1-x). \tag{6.25}$$

Further,

$$c_0^2\frac{\partial}{\partial c}\left(\frac{Z}{\rho}\right) = \frac{k_B T x}{m_4}. \tag{6.26}$$

As noted by Wilks, Khalatnikov has erroneously used the mass concentration in his equations for the entropy of ideal mixtures [109]. The contribution of ^{3}He to the normal fluid density is [107, 109]

$$\rho_{n3} = \rho\frac{m_3^*}{m_4}x, \tag{6.27}$$

where m_3^* is the effective mass of a ^{3}He quasiparticle. The total normal fluid density is

$$\rho_n = \rho_{n3} + \rho_{n4}, \tag{6.28}$$

where ρ_{n4} is the normal fluid density of ^{4}He. It can be approximated by $\xi(1-c)\rho$, where ξ is the normal fluid fraction of pure ^{4}He. It should be noted, however, that with this approximation, the normal fluid density can exceed the density of the liquid, when $\xi \approx 1$. To determine the relevant quantities in the ideal solution approximation, we used experimental data between 1 K and 2.2 K listed in Ref. 109; entropy of pure ^{3}He was from Roberts *et al.* [110], entropy of pure ^{4}He from Kramers *et al.* [111] and Hill and Lounasmaa [112], and the normal

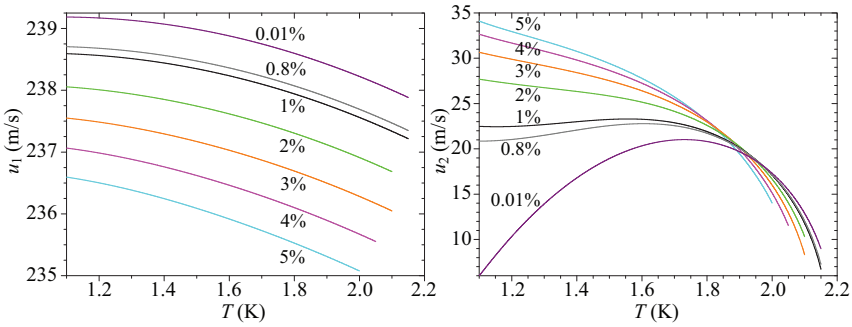

Fig. 6.7 Calculated speeds of first (left figure) and second (right figure) sounds using Eqs. (6.29) and (6.30), the ideal solution model, and experimental data mentioned in the text. The strong decrease in u_2 of pure ^{4}He at $T \lesssim 1.6$ K is contrary to experimental data (Fig. 6.3). The discrepancy is likely due to poor fit to experimental data on the density of ^{4}He at lower temperatures.

fluid fraction of ^{4}He from Ref. 113. Temperature dependence of the density of pure ^{4}He was taken from Ref. 114.

If we consider plane waves, *i.e.* that the deviations vary as $\propto e^{-i\omega(t-z/u)}$, where z is the direction of propagation of the wave and u is the speed of sound, we can determine analytical relations for the speeds of sounds using Eqs. (6.13-6.15). We get two solutions, corresponding to the two sound modes. Ignoring the coefficient of thermal expansion, they are [107]

$$u_1^2 = \left(\frac{\partial P}{\partial \rho}\right)_{c,T} \left[1 + \frac{\rho_\mathrm{s}}{\rho_\mathrm{n}} \left(\frac{\partial \rho}{\partial c}\frac{c}{\rho}\right)^2\right] \tag{6.29}$$

$$u_2^2 = \frac{\rho_\mathrm{s}}{\rho_\mathrm{n}} \left[\bar{\sigma}^2 \left(\frac{\partial T}{\partial \sigma}\right)_{c,P} + c^2 \frac{\partial}{\partial c}\left(\frac{Z}{\rho}\right)\right] \Bigg/ \left[1 + \frac{\rho_\mathrm{s}}{\rho_\mathrm{n}} \left(\frac{\partial \rho}{\partial c}\frac{c}{\rho}\right)^2\right], \tag{6.30}$$

where u_1 is the speed of first sound and u_2 the second sound.

The speeds of first and second sounds obtained by using the ideal solution approximation and Eqs. (6.29) and (6.30) are plotted in Fig. 6.7. Agreement with experimental values is not very good for pure ^{4}He below 1.6 K. This is likely due to poor fit to the experimental data of density as a function of temperature below 1.5 K, mentioned already above. The poor fit was not noticed until the simulations had already been done. This does not, however, change our conclusions in any significant manner. Sound speeds for mixtures are reproduced rather well; they are in the range of measured values.

6.2.2 Simulated quartz tuning fork response

We used the hydrodynamical equations of the previous section and solved them in the quartz tuning fork geometry using the finite element method. Comsol Multiphysics was used again to perform the numerical computations. The quartz tuning fork response was determined in a similar manner as the first sound simulations using an effective harmonic oscillator model described in publication **VI**. The tuning fork was coupled directly only to first sound (pressure) by applying a boundary condition $\hat{n} \cdot \nabla P \neq 0$ on the appropriate tuning fork tine sides. On reflective boundaries all the normal gradients of the variables were set to zero. Small amount of acoustic and thermal impedance (normal gradients equal to some complex number) were applied on the container walls to create finite widths for the resonant modes. Simulated resonant frequency responses of a quartz tuning fork in mixtures with various concentrations are shown in Fig. 6.8. Unlike in the experiments, the second sound resonances in the simulation have not been "tracked", meaning that a constant excitation (measurement) frequency has been applied on the oscillator. We find at least qualitative explanations for the effects observed in publication **VIII** and shown in Fig. 6.3. For pure ^{4}He, the coupling of second sound to first sound is rather modest, and the resulting resonances are extremely narrow. Large number of modes exist at low second sound speeds (short wavelengths), as is expected. The 1.4 K modes in pure ^{4}He seen in Fig. 6.8 are repetitions of the modes at ~ 2.1 K and are due to the unrealistic behavior of u_2 mentioned before. When concentration of ^{3}He is increased, the coupling term becomes small in the important temperature region $T \sim 2$ K, where the strong modes would exist. In our simple model, at 2 K the coupling attains its minimum strength for about 0.8% mixture. Adding ^{3}He also shifts the second sound speed curve to lower temperatures, as T_λ decreases, which results in the modes being shifted to lower temperatures as well. At some point there is enough ^{3}He to increase the second sound speed at lower temperatures enough to bring new resonant modes into view. The coupling is stronger than in pure ^{4}He, so that these modes have more powerful effect on the quartz tuning fork. Since increasing concentration of ^{3}He increases the speed of second sound at temperature below ~ 1.9 K, these mixture modes move to higher temperatures as a function of concentration. During the experiments it was thought that the pure ^{4}He modes disappear completely due to added ^{3}He as they seemed to diminish. Therefore they were not searched for at larger concentrations. Based on the results of our present considerations, we now believe they should reappear, since u_2 goes continuously toward zero when $T \to T_\lambda$ and the coupling between different sound modes increases again.

In our simulations, we also observed a double sound conversion, where first

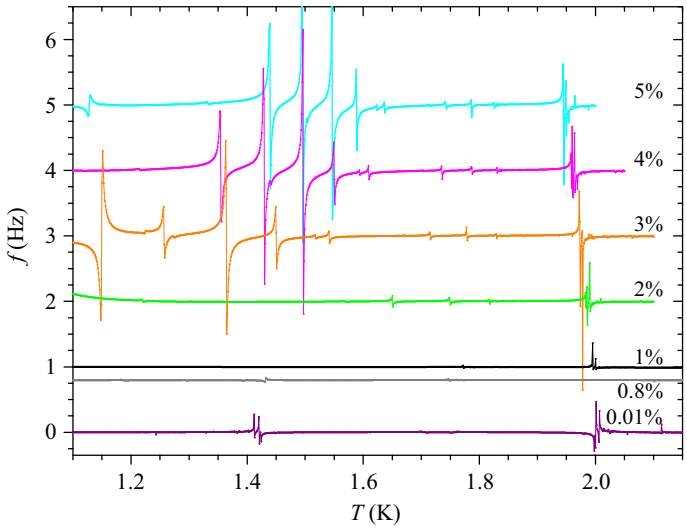

Fig. 6.8 Simulated resonant frequency of an ECS-1x5x quartz tuning fork symmetrically inside a cylindrical cavity with the fluid modeled using the hydrodynamical equations, Eqs. (6.21) and (6.22). A quadratic "background" frequency has been subtracted from each data set to bring out the second sound resonances more clearly. The lines are offset by their respective ^{3}He concentration percentage. These data should be compared to the experimental results shown in Fig. 6.3. The coloring of the curves above are congruent with Figs. 6.3 and 6.6.

sound, excited by the tuning fork, was converted to second sound, which was further converted to first sound and excited resonant modes in the cavity, which are not excited by the tuning fork directly. The coupling of these modes to the tuning fork is very weak, as they must convert back to second sound and again to first sound before being able to affect the resonator. The simulations described in this section are still preliminary and further studies are being conducted.

Chapter 7

Summary and Conclusions

Superfluidity of ^{4}He was apparently reached by Kamerlingh Onnes the same day he liquefied helium for the first time [1]. This phenomenon was not realized until a few decades later, though. Superfluidity of ^{3}He was discovered 60 years later, in 1971. This time the effect was observed right away, but not immediately understood to be the superfluid transition. Now 42 years has passed since then and the last (expected) superfluid state of helium still remains to be discovered. This task is by no means trivial, since direct cooling by adiabatic nuclear demagnetization is limited to around 100 μK by the increasing Kapitza resistance. If the superfluid state of helium mixtures is to be found, the adiabatic melting technique seems to offer about the only possibility to reach it at the moment by yielding perhaps even an order of magnitude lower temperatures than previously achieved. Due to the utmost low temperatures, the measurement setup requires many novel features and even after more than a decade of preparations, the adiabatic melting experiment has not been able to be carried out without clear technical shortcomings.

Our proposed effective interaction potential between ^{3}He quasiparticles in dilute ^{3}He–^{4}He mixtures allows, among other things, estimation of the superfluid transition temperature of mixtures at all pressures and concentrations. This may help in the search for the superfluid state, as it indicates the optimal conditions for the transition. Our estimates for T_c are quite optimistic, since they are in the range of plausible temperatures in the adiabatic melting experiment. The natural pressure of the experiment, the melting pressure of helium mixtures (2.57 MPa), is not quite the optimum pressure according to our results ($T_c \approx 40$ μK), but rather the highest T_c is found between 0.5 MPa and 1 MPa ($T_c \approx 200$ μK) at the saturation concentration.

Helium thermometry at low temperatures is challenging due to the same rea-

son that direct cooling of helium mixtures fails at low temperatures. Thermal boundary resistance prevents a thermometer from reaching the same temperature as the liquid. Following the same philosophy as in the cooling technique, an effective thermometer at low temperatures should somehow probe the properties of the liquid directly. Melting pressure thermometry of helium mixtures offers such a possibility in a similar manner as for pure ^{3}He, which has proven to be very useful. Quartz tuning forks are also sensitive probes, and can be used to rather low temperatures, especially in helium mixtures, where the ^{3}He component remains normal to low temperatures. Approaching the ballistic regime renders such probes insensitive to temperature at around 100 μK. Second sound resonances offer means of constructing a new type of thermometer, capable of extremely good temperature resolution, but only at somewhat higher temperatures.

Our numerical simulations offer better understanding of using quartz tuning fork resonators as probes of liquid helium and their use as thermometers. In most applications, one usually wants to avoid coupling of the oscillator to acoustic resonances in the fluid cavity around the oscillator or within the oscillator geometry. Our results offer guidance in choosing a quartz tuning fork with appropriate dimensions and frequency. To obtain as "ideal" response as possible, here understood as a constant geometrical factor B, one should use small-sized oscillators, lower resonant frequencies, tuning forks as narrow as possible and the tines as close to each other as possible.

The adiabatic melting experiment is being prepared at the moment. While it is under construction, another cell is used to make experiments with helium mixtures. We want to study the solubility, density, and melting pressure of mixtures. We also continue numerical analysis of quartz forks and especially the work on second sound. Path integral Monte Carlo simulations are also being improved and expanded to include many ^{3}He particles.

References

[1] H. Kamerlingh Onnes, Proc. KNAW **11**, 168 (1908).

[2] D. D. Osheroff, R. C. Richardson, and D. M. Lee, Phys. Rev. Lett. **28**, 885 (1972).

[3] J. Bardeen, L. N. Cooper, and J. R. Schrieffer, Phys. Rev. **108**, 1175 (1957).

[4] E. R. Dobbs, *Helium Three* (Oxford University Press, New York, 2000).

[5] D. O. Edwards, D. F. Brewer, P. Seligman, M. Skertic, and M. Yaqub, Phys. Rev. Lett. **15**, 773 (1965).

[6] G.-H. Oh, Y. Ishimoto, T. Kawae, M. Nakagawa, O. Ishikawa, T. Hata, T. Kodama, and S. Ikehata, J. Low Temp. Phys. **95**, 525 (1994).

[7] J. Tuoriniemi, J. Martikainen, E. Pentti, A. Sebedash, S. Boldarev, and G. Pickett, J. Low Temp. Phys. **129**, 531 (2002).

[8] D. O. Edwards and M. S. Pettersen, J. Low Temp. Phys. **87**, 473 (1992).

[9] R. Rusby, M. Durieux, A. Reesink, R. Hudson, G. Schuster, M. Kühne, W. Fogle, R. Soulen, and E. Adams, J. Low Temp. Phys. **126**, 633 (2002).

[10] D. O. Clubb, O. V. L. Buu, R. M. Bowley, R. Nyman, and J. R. Owers-Bradley, J. Low Temp. Phys. **136**, 1 (2004).

[11] R. Blaauwgeers, M. Blazkova, M. Clovecko, V. Eltsov, R. de Graaf, J. Hosio, M. Krusius, D. Schmoranzer, W. Schoepe, L. Skrbek, P. Skyba, R. Solntsev, and D. Zmeev, J. Low Temp. Phys. **146**, 537 (2007).

[12] F. Pobell, *Matter and Methods at Low Temperatures*, 3rd ed. (Springer, Berlin, 2007).

[13] A. P. Sebedash, J. T. Tuoriniemi, S. T. Boldarev, E. M. M. Pentti, and A. J. Salmela, J. Low Temp. Phys. **148**, 725 (2007).

[14] L. Landau, Zh. Eksp. Teor. Fiz. **30**, 1058 (1956).

[15] G. Baym and C. Pethick, *Landau Fermi-Liquid Theory* (John Wiley, New York, 1991).

[16] J. F. Annett, *Superconductivity, Superfluids, and Condensates* (Oxford University Press, New York, 2004).

[17] A. L. Fetter and J. D. Walecka, *Quantum Theory of Many-Particle Systems* (Dover, New York, 2003).

[18] J. R. Owers-Bradley, P. C. Main, and R. M. Bowley, J. Low Temp. Phys. **72**, 201 (1988).

[19] J. Bardeen, G. Baym, and D. Pines, Phys. Rev. **156**, 207 (1967).

[20] G. E. Watson, J. D. Reppy, and R. C. Richardson, Phys. Rev. **188**, 384 (1969).

[21] E. M. Pentti, J. T. Tuoriniemi, A. J. Salmela, and A. P. Sebedash, Phys. Rev. B **78**, 064509 (2008).

[22] P. W. Anderson and P. Morel, Phys. Rev. **123**, 1911 (1961).

[23] R. Balian and N. R. Werthamer, Phys. Rev. **131**, 1553 (1963).

[24] C. Ebner, Phys. Rev. **156**, 222 (1967).

[25] S. Yorozu, M. Hiroi, H. Fukuyama, H. Akimoto, H. Ishimoto, and S. Ogawa, Phys. Rev. B **45**, 12942 (1992).

[26] J. C. Owen, Phys. Rev. Lett. **47**, 586 (1981).

[27] W. Hsu and D. Pines, J. Stat. Phys. **38**, 273 (1985).

[28] T. Soda, Prog. Theor. Phys. **90**, 353 (1993).

[29] B. R. Patton and A. Zaringhalam, Phys. Lett. **55A**, 95 (1975).

[30] D. Fay, Phys. Rev. B **16**, 537 (1977).

[31] E. P. Bashkin and A. E. Meyerovich, Adv. Phys. **30**, 1 (1981).

[32] P. G. van de Haar, G. Frossati, and K. S. Bedell, J. Low Temp. Phys. **77**, 35 (1989).

[33] M. Nakamura, Y. Fujii, M. Yamamoto, M. Kinoshita, and M. Yamaguchi, J. Low Temp. Phys. **129**, 43 (2002).

[34] D. S. Greywall, Phys. Rev. B **27**, 2747 (1983).

[35] D. S. Greywall, Phys. Rev. B **33**, 7520 (1986).

[36] B. M. Abraham and D. W. Osborne, J. Low Temp. Phys. **5**, 335 (1971).

[37] B. M. Abraham, D. Chung, Y. Eckstein, J. B. Ketterson, and P. R. Roach, J. Low Temp. Phys. **6**, 521 (1972).

[38] D. O. Edwards, E. M. Ifft, and R. E. Sarwinski, Phys. Rev. **177**, 380 (1969).

[39] R. A. Sherlock and D. O. Edwards, Phys. Rev. A **8**, 2744 (1973).

[40] D. S. Greywall, Phys. Rev. B **20**, 2643 (1979).

[41] M. Boninsegni and D. M. Ceperley, Phys. Rev. Lett. **74**, 2288 (1995).

[42] R. Simons and R. M. Mueller, Czech. J. Phys. **46**, 201 (1996).

[43] E. Krotscheck, M. Saarela, K. Schörkhuber, and R. Zillich, Phys. Rev. Lett. **80**, 4709 (1998).

[44] D. O. Edwards and S. Balibar, Phys. Rev. B **39**, 4083 (1989).

[45] D. O. Edwards, M. S. Pettersen, and T. G. Culman, J. Low Temp. Phys. **89**, 831 (1992).

[46] J. He, T. G. Culman, H. H. Hjort, and D. O. Edwards, Phys. Rev. Lett. **80**, 3292 (1998).

[47] J. P. Laheurte, J. Low Temp. Phys. **12**, 127 (1973).

[48] W. F. Saam and J. P. Laheurte, Phys. Rev. A **4**, 1170 (1971).

[49] F. A. de Saavedra, J. Boronat, A. Polls, and A. Fabrocini, Phys. Rev. B **50**, 4248 (1994).

[50] E. R. Grilly, J. Low Temp. Phys. **4**, 615 (1971).

[51] E. R. Grilly, J. Low Temp. Phys. **11**, 33 (1973).

[52] A. Driessen, E. van der Poll, and I. F. Silva, Phys. Rev. B **33**, 3269 (1986).

[53] W. P. Halperin, F. B. Rasmussen, C. N. Archie, and R. C. Richardson, J. Low Temp. Phys. **31**, 617 (1978).

[54] R. A. Scribner, M. F. Panczyk, and E. D. Adams, J. Low Temp. Phys. **1**, 313 (1969).

[55] B. A. Fraass and R. O. Simmons, Phys. Rev. B **36**, 97 (1987).

[56] V. N. Lopatik, JETP **59**, 284 (1984).

[57] B. van den Brandt, W. Griffioen, G. Frossati, H. van Beelen, and R. de Bruyn Ouboter, Physica **114B**, 295 (1982).

[58] P. M. Tedrow and D. M. Lee, Phys. Rev. **181**, 399 (1969).

[59] V. L. Vvedenskii, JETP Lett. **24**, 133 (1976).

[60] M. S. Manninen, H. J. Junes, J.-P. Kaikkonen, A. Y. Parshin, I. A. Todoshchenko, and V. Tsepelin, J. Phys. Conf. Ser. **150**, 012026 (2009).

[61] E. C. Kerr and R. H. Sherman, J. Low Temp. Phys. **3**, 451 (1970).

[62] R. P. Feynman and A. R. Hibbs, *Quantum Mechanics and Path Integrals* (Dover, New York, 2010).

[63] L. E. Reichl, *A Modern Course in Statistical Physics* (John Wiley, New York, 1998).

[64] D. M. Ceperley, J. Stat. Phys. **63**, 1237 (1991).

[65] R. A. Aziz, A. R. Janzen, and M. R. Moldover, Phys. Rev. Lett. **74**, 1586 (1995).

[66] D. M. Ceperley, Rev. Mod. Phys. **67**, 279 (1995).

[67] Software Archive - Materials Computation Center, University of Illinois at Urbana-Champaign, `http://www.mcc.uiuc.edu/software/`, April 2013.

[68] J. Boronat and J. Casulleras, Phys. Rev. B **59**, 8844 (1999).

[69] Y. Wang and P. E. Sokol, Phys. Rev. Lett. **72**, 1040 (1994).

[70] R. T. Azuah, W. G. Stirling, J. Mayers, I. F. Bailey, and P. E. Sokol, Phys. Rev. B **51**, 6780 (1995).

[71] R. Senesi, C. Andreani, A. L. Fielding, J. Mayers, and W. G. Stirling, Phys. Rev. B **68**, 214522 (2003).

[72] C. Andreani, C. Pantalei, and R. Senesi, J. Phys.: Condens. Matter **18**, 5587 (2006).

[73] M. Boninsegni and S. Moroni, Phys. Rev. Lett. **78**, 1727 (1997).

[74] J. Boronat, A. Polls, and A. Fabrocini, Phys. Rev. B **56**, 11854 (1997).

[75] C. Ebner and D. O. Edwards, Phys. Rep. **1**, 77 (1971).

[76] J. T. Tough, W. D. McCormick, and J. G. Dash, Phys. Rev. **132**, 2373 (1963).

[77] D. Bradley, S. Fisher, A. Guenault, R. Haley, M. Holmes, S. O'Sullivan, G. Pickett, and V. Tsepelin, J. Low Temp. Phys. **150**, 364 (2008).

[78] J. Jäger, B. Schuderer, and W. Schoepe, Phys. Rev. Lett. **74**, 566 (1995).

[79] M. Blažková, M. Človečko, V. Eltsov, E. Gažo, R. de Graaf, J. Hosio, M. Krusius, D. Schmoranzer, W. Schoepe, L. Skrbek, P. Skyba, R. Solntsev, and W. Vinen, J. Low Temp. Phys. **150**, 525 (2008).

[80] M. Blažková, M. Človečko, E. Gažo, L. Skrbek, and P. Skyba, J. Low Temp. Phys. **148**, 305 (2007).

[81] D. Rainer and J. W. Serene, Phys. Rev. B **13**, 4745 (1976).

[82] I. A. Todoschenko, H. Alles, A. Babkin, A. Y. Parshin, and V. Tsepelin, J. Low Temp. Phys. **126**, 1446 (2002).

[83] T. H. Virtanen and E. Thuneberg, Phys. Rev. Lett. **106**, 055301 (2011).

[84] T. H. Virtanen and E. V. Thuneberg, Phys. Rev. B **83**, 224521 (2011).

[85] K. Karrai and R. Grober, Proc. SPIE **2535**, 69 (1995).

[86] D. L. Shuster and K. A. Farley, Geochim. Cosmochim. Acta **69**, 2349 (2005).

[87] G. G. Boiko and G. V. Berezhnoi, Glass Phys. Chem. **29**, 42 (2003).

[88] D. Schmoranzer, M. La Mantia, G. Sheshin, I. Gritsenko, A. Zadorozhko, M. Rotter, and L. Skrbek, J. Low Temp. Phys. **163**, 317 (2011).

[89] I. Gritsenko, A. Zadorozhko, and G. Sheshin, J. Low Temp. Phys. **171**, 194 (2013).

[90] E. Pentti, J. Tuoriniemi, A. Salmela, and A. Sebedash, J. Low Temp. Phys. **150**, 555 (2008).

[91] P. Kapitza, Nature **141**, 74 (1938).

[92] J. F. Allen and A. D. Misener, Nature **141**, 75 (1938).

[93] J. F. Allen and H. Jones, Nature **141**, 243 (1938).

[94] S. Balibar, J. Low Temp. Phys. **146**, 441 (2007).

[95] L. Tisza, Nature **141**, 913 (1938).

[96] L. Tisza, Comptes Rendus Acad. Sc. **207**, 1035 (1938).

[97] L. Tisza, Comptes Rendus Acad. Sc. **207**, 1186 (1938).

[98] L. D. Landau, Phys. Rev. **60**, 356 (1941).

[99] L. D. Landau, J. Phys. USSR **5**, 71 (1941).

[100] C. T. Lane, H. A. Fairbank, and W. M. Fairbank, Phys. Rev. **71**, 600 (1947).

[101] R. D. Maurer and M. A. Herlin, Phys. Rev. **76**, 948 (1949).

[102] D. de Klerk, R. P. Hudson, and J. R. Pellam, Phys. Rev. **93**, 28 (1954).

[103] J. C. King and H. A. Fairbank, Phys. Rev. **93**, 21 (1954).

[104] N. R. Brubaker, D. O. Edwards, R. E. Sarwinski, P. Seligmann, and R. A. Sherlock, J. Low Temp. Phys. **3**, 619 (1970).

[105] L. D. Landau and E. M. Lifshitz, *Fluid Mechanics*, 2nd ed. (Pergamon Press, Oxford, 1987).

[106] S. J. Putterman, *Superfluid Hydrodynamics* (North-Holland, Amsterdam, 1974).

[107] I. M. Khalatnikov, *An Introduction to the Theory of Superfluidity* (Westview Press, New York, 2000).

[108] P. Brusov, J. M. Parpia, P. Brusov, and G. Lawes, Phys. Rev. B **63**, 140507 (2001).

[109] J. Wilks, *The Properties of Liquid and Solid Helium* (Clarendon Press, Oxford, 1967).

[110] T. R. Roberts, R. H. Sherman, S. G. Sydoriak, and F. G. Brickwedde, Prog. Low Temp. Phys. **4**, 480 (1964).

[111] H. C. Kramers, J. D. Wasscher, and C. J. Gorter, Physica **18**, 329 (1952).

[112] R. W. Hill and O. V. Lounasmaa, Phil. Mag. **2**, 143 (1957).

[113] A. D. B. Woods and A. C. H. Hallett, Can. J. Phys. **41**, 596 (1963).

[114] J. J. Niemela and R. J. Donnelly, J. Low Temp. Phys. **98**, 1 (1995).

Aalto-DD 110/2013

ISBN 978-952-60-5244-1
ISBN 978-952-60-5245-8 (pdf)
ISSN-L 1799-4934
ISSN 1799-4934
ISSN 1799-4942 (pdf)

Aalto University
School of Science
O.V. Lounasmaa Laboratory
www.aalto.fi

BUSINESS +
ECONOMY

ART +
DESIGN +
ARCHITECTURE

SCIENCE +
TECHNOLOGY

CROSSOVER

DOCTORAL
DISSERTATIONS